Brain, Behavior, and Immunity 109 (2023) 1–22

Contents lists available at ScienceDirect

Brain Behavior and Immunity

journal homepage: www.elsevier.com/locate/ybrbi

Full-length Article

Selective PDE4 subtype inhibition provides new opportunities to intervene in neuroinflammatory versus myelin damaging hallmarks of multiple sclerosis

Melissa Schepers [a,b,c], Dean Paes [a,b], Assia Tiane [a,b,c], Ben Rombaut [a,b], Elisabeth Piccart [a], Lieve van Veggel [a,b,c], Pascal Gervois [d], Esther Wolfs [d], Ivo Lambrichts [d], Chiara Brullo [e], Olga Bruno [e], Ernesto Fedele [f,g], Roberta Ricciarelli [g,h], Charles ffrench-Constant [i], Marie E. Bechler [j], Pauline van Schaik [k], Wia Baron [k], Evy Lefevere [l], Kobi Wasner [m], Anne Grünewald [m], Catherine Verfaillie [n], Paulien Baeten [c,o], Bieke Broux [c,o], Paul Wieringa [p], Niels Hellings [c,o], Jos Prickaerts [b,1], Tim Vanmierlo [a,b,c,*,1]

[a] Department of Neuroscience, Biomedical Research Institute, Faculty of Medicine and Life Sciences, Hasselt University, Diepenbeek, Belgium
[b] Department Psychiatry and Neuropsychology, School for Mental Health and Neuroscience, Maastricht University, Maastricht, Netherlands
[c] University MS Center (UMSC) Hasselt-Pelt, Hasselt, Belgium
[d] Department of Cardio and Organ Systems, Biomedical Research Institute, Hasselt University, Diepenbeek, Belgium
[e] Department of Pharmacy, Section of Medicinal Chemistry, University of Genoa, Genova, Italy
[f] Department of Pharmacy, Section of Pharmacology and Toxicology, University of Genova, Genova, Italy
[g] IRCCS Ospedale Policlinico San Martino, Genova, Italy
[h] Department of Experimental Medicine, Section of General Pathology, University of Genova, Genova, Italy
[i] MRC Centre for Regenerative Medicine and MS Society Edinburgh Centre, Edinburgh bioQuarter, University of Edinburgh, Edinburgh, UK
[j] Department of Cell and Developmental Biology, SUNY Upstate Medical University, Syracuse, NY, USA
[k] Department of Biomedical Sciences of Cells and Systems, Section Molecular Neurobiology, University of Groningen, University Medical Center Groningen, Groningen, the Netherlands
[l] Rewind Therapeutics NV, Gaston Geenslaan 2, B-3001, Leuven, Belgium
[m] Luxembourg Centre for Systems Biomedicine, University of Luxembourg, Esch-sur-Alzette, Luxembourg
[n] Stem Cell Institute, Department of Development and Regeneration, KU Leuven, Belgium
[o] Department of Immunology and Infection, Biomedical Research Institute, Hasselt University, Diepenbeek, Belgium
[p] MERLN Institute for Technology-Inspired Regenerative Medicine, Complex Tissue Regeneration department, Maastricht University, Maastricht, the Netherlands

ARTICLE INFO

Keywords:
Multiple sclerosis
Phosphodiesterases
Remyelination
Neuroinflammation

ABSTRACT

Multiple sclerosis (MS) is a chronic autoimmune disease of the central nervous system (CNS) characterized by focal inflammatory lesions and prominent demyelination. Even though the currently available therapies are effective in treating the initial stages of disease, they are unable to halt or reverse disease progression into the chronic progressive stage. Thus far, no repair-inducing treatments are available for progressive MS patients. Hence, there is an urgent need for the development of new therapeutic strategies either targeting the destructive immunological demyelination or boosting endogenous repair mechanisms. Using *in vitro*, *ex vivo,* and *in vivo* models, we demonstrate that selective inhibition of phosphodiesterase 4 (PDE4), a family of enzymes that hydrolyzes and inactivates cyclic adenosine monophosphate (cAMP), reduces inflammation and promotes myelin repair. More specifically, we segregated the myelination-promoting and anti-inflammatory effects into a PDE4D- and PDE4B-dependent process respectively. We show that inhibition of PDE4D boosts oligodendrocyte progenitor cells (OPC) differentiation and enhances (re)myelination of both murine OPCs and human iPSC-derived OPCs. In addition, PDE4D inhibition promotes *in vivo* remyelination in the cuprizone model, which is accompanied by improved spatial memory and reduced visual evoked potential latency times. We further identified that PDE4B-specific inhibition exerts anti-inflammatory effects since it lowers *in vitro* monocytic nitric oxide (NO) production and improves *in vivo* neurological scores during the early phase of experimental autoimmune

* Corresponding author.
E-mail addresses: t.vanmierlo@maastrichtuniversity.nl, tim.vanmierlo@uhasselt.be (T. Vanmierlo).
[1] These authors contributed equally.

https://doi.org/10.1016/j.bbi.2022.12.020
Received 14 September 2022; Received in revised form 17 December 2022; Accepted 24 December 2022
Available online 28 December 2022

encephalomyelitis (EAE). In contrast to the pan PDE4 inhibitor roflumilast, the therapeutic dose of both the PDE4B-specific inhibitor A33 and the PDE4D-specific inhibitor Gebr32a did not trigger emesis-like side effects in rodents. Finally, we report distinct *PDE4D* isoform expression patterns in human area postrema neurons and human oligodendroglia lineage cells. Using the CRISPR-Cas9 system, we confirmed that *pde4d1/2* and *pde4d6* are the key targets to induce OPC differentiation. Collectively, these data demonstrate that gene specific PDE4 inhibitors have potential as novel therapeutic agents for targeting the distinct disease processes of MS.

1. Introduction

The chronic autoimmune disease multiple sclerosis (MS) is characterized by the infiltration of myelin-reactive *T*-cells, B-cells, and infiltrating macrophages in the central nervous system (CNS) (Lucchinetti et al., 1996; Wucherpfennig et al., 1992; Prineas and Wright, 1978). Subsequent pathological processes encompass chronic inflammation, demyelination of the axons, and loss of myelin producing oligodendrocytes (Weiner, 2009; Compston and Coles, 2008). In relapse-remitting MS (RRMS), spontaneous remyelination occurs by differentiation of recruited oligodendrocyte progenitor cells (OPCs) into myelin-producing oligodendrocytes (Ansi Chang et al., 2002; Kotter et al., 2011; Charles, 2008; Zawadzka et al., 2010). Although abundantly present in many CNS lesions, OPCs eventually fail to differentiate into mature myelinating oligodendrocytes. This failure and incomplete remyelination are features of progressive MS (PMS) (Ansi Chang et al., 2002; Kuhlmann et al., 2008; Wolswijk, 1998). Early disease activity in RRMS patients is suppressed by immunomodulatory treatment strategies that aim to suppress the autoimmune-induced demyelination (Wingerchuk and Carter, 2014; Henze et al., 2006). Yet, in spite of treatment, about 50 % of the RRMS patients will develop into secondary PMS patients within a time frame of 10 to 15 years following disease onset (Trojano et al., 2003; Ontaneda et al., 2017). Additionally, approximately 10–15 % of MS patients endure gradual accumulation of disability from disease onset, without experiencing an initial relapsing course. These patients are classified as primary PMS patients (Ontaneda et al., 2017). During the early stages of PMS, treatments such as ocrelizumab and siponimod are still effective as they suppress the overactive immune system (Wolinsky et al., 2020; Kappos et al., 2018). However, as the disease progresses, no approved therapy has been shown effective in restoring the damaged myelin or neurons in the CNS (Bear and Paradiso, 2007).

3′-5′-cyclic adenosine monophosphate (cAMP) has been described to possess prominent immunomodulatory and myelin regenerative functions (Raible and McMorris, 1989; Mosenden and Tasken, 2011). Phosphodiesterases (PDEs) catalyze the hydrolysis of second messengers such as cAMP and cGMP to regulate the spatiotemporal presence and activity of second messengers intracellularly. PDEs comprise eleven enzyme families (PDE1-11) that hydrolyze the cyclic nucleotides cAMP and/or cGMP. The PDE4 family is the most prominently expressed cAMP-specific PDE family in immune cells and oligodendrocytes. The four different PDE4 subtypes (PDE4A, B, C and D) each encodes for multiple transcriptional variants (e.g., PDE4D1-PDE4D9) (Whitaker et al., 2008; Braun et al., 2007; Ugarte et al., 2015; Richter et al., 2013; Houslay, 2010; Paes et al., 2021). The generated PDE4D isoforms share a particular amino acid similarity (upstream conserved region (UCR) 1, UCR2 partially and the catalytic domain), but can be distinguished based on their unique *N*-terminal amino acid sequence (Bolger, 1994; Johnson et al., 2010). PDE4 isoforms can be categorized as long, short or supershort based on the inclusion of both the UCR1 and UCR2, UCR2 only or a truncated UCR2 region as regulatory domains (Peng et al., 2020). The molecular biology of the different PDE4 enzymes is described and visualized extensively by Paes et al. (Paes et al., 2021). Indeed, several preclinical studies have shown the efficacy of different pan PDE4 inhibitors for diminishing neuroinflammation in experimental autoimmune encephalitis (EAE) and enhancing remyelination in the cuprizone model, which are two well-established animal models of MS (Bielekova et al., 2000; Bielekova et al., 2009; Syed et al., 2013). Recently, a phase II double-blinded clinical trial with the small molecule ibudilast, which inhibits PDE4 as well as PDE10, toll-like-receptor-4 (TLR4) and the macrophage migration factor (MIF), demonstrated a 48 % reduction in brain parenchymal fraction in PMS patients indicating a reduction in brain atrophy (Fox et al., 2016; Fox et al., 2018). Although generally well tolerated, patients treated with ibudilast did report a higher incidence of gastrointestinal disorders (Fox et al., 2016; Fox et al., 2018). In line, clinical studies with pan PDE4 inhibitors were prematurely terminated due to adverse events such as vomiting, nausea, and gastroesophageal reflexes (Bielekova et al., 2009; Sanabra et al., 2013). Interestingly, PDE4 genes (e.g. *PDE4A-D*) and isoforms (e.g. *PDE4B1-PDE4B5* and *PDE4D1-PDE4D9*) show distinct cellular expression patterns and intracellular compartmentalization, and can therefore offer a more targeted approach for controlling neuro-inflammation, neuro-regeneration, and remyelination, thereby enhancing the therapeutic potential and diminishing side effects accompanied with pan PDE4 inhibition (Paes et al., 2021; Blokland et al., 2019).

To overcome the emetic effects of full PDE4 inhibitors, yet maintain the anti-inflammatory and regenerative potential, PDE4 subtype inhibition can be considered unique therapeutic targets. PDE4B has been described to be primarily related to the modulation of inflammatory responses (Sanabra et al., 2013; Jin et al., 2005; Myers et al., 2019; Reyes-Irisarri et al., 2007). As such, *pde4b* expression is highly increased in monocytes upon inflammatory stimulation. PDE4B inhibition has been shown to promote phosphorylation and thus mediate activation of STAT3 (signal transducer and activator of transcription 3) (Yang et al., 2017). In infiltrated regulatory T cells, the negative correlation found between *pde4b2, FoxP3* and TGF-β levels, suggest an immunomodulatory role of PDE4B2 (Sanabra et al., 2013; Reyes-Irisarri et al., 2007; Sonar and Lal, 2017). On the contrary, the PDE4D-sparing PDE4 inhibitor ABI-4 did not affect inflammatory processes in murine microglia cultures, excluding a direct role for PDE4D in inflammation (Hedde et al., 2017). Alternatively, PDE4D-specific inhibition has been largely related to improved memory and neuroplasticity (Mohammadnejad et al., 2021; Xiang et al., 2020; Zhang et al., 2017; Shi et al., 2021; Zhang et al., 2014; Sierksma et al., 2014; Cui et al., 2019). However, despite being a therapeutic target, it is hypothesized that especially PDE4D is responsible for the emetic side effects upon pan PDE4 inhibition since *PDE4D* is highly expressed in the area postrema, the chemoreceptor trigger zone for emesis in the brainstem, compared to other PDE4 genes (Mori et al., 2010). In line, complete *PDE4D* gene deletion resulted in increased emetic-like behavior in rodents (Mori et al., 2010; Robichaud et al., 2002). Yet, the second generation PDE4 inhibitor roflumilast showed less emetic side effects compared to the first generation PDE4 inhibitor rolipram, and, interestingly, PDE4D-specific inhibitors such as Gebr7b, Gebr32a and BPN14770 did not result in emesis up to 100-fold of their effective memory enhancing dose (Vanmierlo et al., 2016; Bruno et al., 2011; Ricciarelli et al., 2017; Zhang et al., 2018). The reduced emetogenic potential in these new generation PDE4(D) inhibitors is likely due to the different affinity for the individual *PDE4D* isoforms expressed in the area postrema, as distinct isoforms show specific intracellular localization indicating different biological roles (Paes et al., 2021).

Consequently, we hypothesized that by selectively targeting PDE4 gene products, i.e., specifically PDE4D and PDE4B, the therapeutic potential of PDE4 inhibition in relation to MS can be specifically directed

towards remyelination or inflammation, without triggering emetic side effects. In this study, we show that selective inhibition of PDE4D increased OPC differentiation and remyelination. We further demonstrate distinct *pde4d* isoform expression profiles in human area postrema neurons and human MS oligodendroglia lineage cells. Moreover, we demonstrate that targeting PDE4B halts inflammatory damage by suppressing neuro-inflammatory responses in the EAE animal model of MS without affecting remyelination. Interestingly, the therapeutic dosage of both the PDE4B inhibitor (A33) or PDE4D inhibitor (Gebr32a) did not show emetic side effects in the xylazine-ketamine wake-up test, a surrogate test for emesis in rodents, nor did it increase the *ex vivo* action potential firing rate of neurons in the murine area postrema. To our knowledge, this is the first study demonstrating that selective PDE4D and PDE4B inhibition provides new opportunities to safely intervene in either the myelin damaging or the neuro-inflammatory hallmarks of MS to induce CNS repair.

2. Materials and methods

2.1. Animals

For EAE induction, 10-week old female C57BL/6J OlaHsd mice were obtained from Envigo (the Netherlands) and were housed in groups upon arrival. For the cuprizone experiment, eight-week old male C57BL/6J OlaHsd mice were obtained from Envigo (the Netherlands) and were housed individually. All animals were housed in a controlled temperature environment (21–22 °C) with an inverse day-night rhythm (lights off 7a.m., lights on 7p.m) and ad libitum access to food and water. A radio, which was playing softly, provided background noise in the room. The experiments were conducted in accordance to the guidelines of EU Directive 2010/63/EU on the protection of animals used for scientific purposes. All experiments were approved by the local ethical committee at Hasselt University for animal experiments (matrix ID: 201551; 201652; 201836; 201976; 202035).

2.2. Cuprizone

After one week of acclimatization, male C57BL/6J OlaHsd mice were subjected to a cuprizone or control diet. Cuprizone (Bis(cyclohexanone) oxaldihydrazone) (Sigma- Aldrich, United States) was mixed at an 0.3 % w/w end concentration in crushed chow. Weight changes were monitored daily throughout the experiment. Treatment was initiated two days preceding the cuprizone stop, and continued for 9 additional days. At the end of the experiment, animals were sacrificed via transcardial perfusion (PBS/heparin) after lethal dolethal injection (200 mg/kg). Brains were collected and post-mortem fixated via overnight 4 % PFA immersion. After immersion, a sucrose gradient was used for cryoprotection (10 %, 20 %, 30 %) after which brains were frozen in liquid nitrogen.

2.3. Roflumilast, A33 and Gebr32a treatment

Where indicated, animals received a twice a day subcutaneous injection containing roflumilast (1 mg/kg or 3 mg/kg) (BioLeaders)(IC_{50} PDE4: 0.2–4.3 nM (Hatzelmann et al., 2010), Gebr32a (0.1 mg/kg or 0.3 mg/kg) (University of Genova) (IC_{50} PDE4D isoforms: 1.16–4.97 μM (Ricciarelli et al., 2017), or A33 (3 mg/kg) (Sigma-Aldrich) (IC_{50} PDE4B: 27 nM (Fox et al., 2014) dissolved in DMSO (1:1000; vehicle) (VWR prolabo) (Ricciarelli et al., 2017; Wilson et al., 2017). Compounds were further diluted in 0.5 % methylcellulose and 2 % Tween80.

2.1.1. Functional readout

2.1.1.1. Object location task

The object location task (OLT) was performed during the pre-motoric phase of the EAE (4 and 10 d.p.i) and during the cuprizone experiment (during demyelination phase (6weekscuprizone) and remyelination phase (5dayspostcuprizone)). Baseline performance was assessed following acclimatization and preceding the start of the experiments. The OLT was performed as described previously (Vanmierlo et al., 2011). Briefly, animals were placed in a circular arena with a diameter and height of 40 cm. The back-half of the arena wall was made of polyvinyl chloride covered with white paper. Testing was performed during two trials of 4 min (trial 1 with symmetrically placed objects; trial 2 with one stationary and one moved object). The exploration time for the two objects was measured manually using self-designed object location task software. The measures were used to calculate the discrimination index (d2 = (time spent on moved object – time spent on object on former place)/time spent exploring in trial 2). A d2 > 0 indicates a preference for the moved object, while a d2 that is not significantly different from 0 indicates no preference. All behavioral experiments were performed in a randomized blinded setup.

2.1.1.2. Visual evoked potential

Epidermal visual evoked potentials (VEPs) were measured at the end of the cuprizone-induced demyelination phase (6weeksofcuprizone) and during remyelination (4dayspostcuprizone). Animals were dark-adapted for at least 3 h prior to the start of VEP to increase sensitivity and to provide a larger dynamic range. Any light sources in the room (laptop, digital scale) were covered with infrared filters. Animals were anesthetized by intraperitoneal (i.p.) injection with xylazine (20 mg/kg) and ketamine (80 mg/kg). Pupils were dilated using 1 % tropicamide for 5 min, and subsequently 2.5 % phenylephrine hydrochloride for 1 min. Next, mice were placed on a heating pad and an active electrode was placed subdermal at the visual cortex, a ground electrode was inserted at the base of the tail to prevent electromagnetic noise from the environment, and finally, a reference electrode was inserted in the tongue. Lastly, the eyes were moistened with saline and the flash electrodes were placed on the eyes. Impedance measurement was used to evaluate electrode connection before starting the VEP. Next, mice were presented with 200 white light flashes, each with a duration of 310 ms. The stimulus frequency was set at 1 Hz and stimulus intensity was set at 0.5 $cd.s/m^2$. Latency time (i.e. time between visual flash stimulus and the arrival of the signal in the visual cortex) was given in milliseconds (ms) being reflective of the myelination status of the visual tract.

2.1.1.3. Experimental autoimmune encephalomyelitis (EAE)

Mice were immunized subcutaneously with an emulsion containing 300 μg myelin oligodendrocyte glycoprotein 35–55 peptide (MOG35–55) in complete Freund's adjuvant (CFA) (0.5–1.5 mg killed mycobacterium tuberculosis) (EK-2110) and received two intraperitoneal (i.p.) injections of pertussis toxin (PTX) directly after immunization and 24 h later (100 ng/injection) (Hooke). For the bone marrow transplantation EAE experiment, only one PTX injection was administered (40 ng/injection) (Hooke). Animal welfare was monitored daily while being clinically scored by blinded investigators using a standard 5-point scale (0: no symptoms; 1: limp tail; 2: hind limp weakness; 3: complete hind limp paralysis; 4: complete hind limp paralysis and partial front leg paralysis; 5: moribund). Animals were sacrificed at EAE onset (n = 5/group), peak (n = 5/group) and at the end of the experiment (n=≥8/group) by transcardial perfusion following a lethal Dolethal injection (200 mg/kg). The brain, spinal cord, spleen and lymph nodes were harvested from each animal. The lymph nodes, spleen and CNS (1brainhemisphereandhalfofthespinalcord) were further processes for flow cytometry analysis. The remaining part of the spinal cord was imbedded in Tissue-Tek optimal cutting temperature (OCT) compound (IHC) and together with the brain (qPCR) snap-frozen using liquid nitrogen.

2.1.1.4. Bone marrow transplantation

Chimeric mice were generated by whole body irradiation (eight Gy) of C57BL/6 females. Femurs and tibias were removed from female

pde4b$^{+/+}$, *pde4b*$^{+/-}$ and *pde4b*$^{-/-}$ mice (*pde4b*$^{-/-}$ mice kindly provided by Prof. Dr. Viacheslav). *Pde4b*$^{-/-}$ is generated by homologous recombination, as described previously (Bailey et al., 1996). Bone marrow was flushed with sterile PBS (phosphate buffered saline, pH: 7.5). Mice were reconstituted with 10^7 cells into the tail vein of recipients within 4 h post-irradiation. Bone marrow was allowed to engraft for 9 weeks before EAE induction. During recovery, mice were treated with Neomycin (FSA Chemicals) and Polymyxini B sulphate (Fagron) added to the drinking water.

2.2.1. Human derived cell culture

2.2.1.1. Human monocyte derived macrophages

Human-derived monocytes were sorted using the MojoSortTM Streptavidin Nanobeads Column Protocol and positive selection. The positively sorted CD14$^+$ cells were re-suspended in RPMI 1640 medium (Lonza) supplemented with 10 % fetal bovine serum and 50 U/ml penicillin and 50 mg/ml streptomycin (all Life technologies). Cells were plated at a density of 1.4×10^5 cells per well in 24-well plates and placed in a humidified CO_2 incubator at 5 % CO_2/ 37 °C for 7 days. Thereafter, cells were treated with vehicle (0.1 % DMSO), the PDE4 inhibitor roflumilast (1 μM), the PDE4B inhibitor A33 (1 μM) or the PDE4D inhibitor Gebr32 (1 μM), and exposed to isolated human myelin (100 μg/ml). Subsequently, after 24 h, macrophages were treated with pro-inflammatory stimuli (10 ng/ml IL-1β and 100 ng/ml IFN-γ) (PeproTech) for another 24 h.

2.2.1.2. iPSC-derived OPCs

Inducible SOX10 overexpressing iPSCs were generated from the human iPSC Sigma line (iPSC EPITHELIAL-1 IPSC0028, purchased from Sigma-Aldrich, ECACC cat. no. 66540499) and used to obtain O4$^+$ and MBP$^+$ oligodendrocyte culture as described previously (Garcia-Leon et al., 2020; Neyrinck and Garcia-Leon, 2021). After differentiating iPSCs towards oligodendrocytes, cells were frozen in liquid nitrogen until thawing of the cells for the microfiber myelination assay. Throughout the myelination assay, cells were kept in iPSC oligodendrocyte differentiation medium (see Supplementary table S1 for medium composition).

2.3.1. Primary murine cell isolation

2.3.1.1. Oligodendrocyte precursor cells

Primary mouse oligodendrocyte precursor cells (OPCs) were isolated from p0 C57bl6 pups using the shake off method as described previously (Tiane et al., 2021). Primary OPCs were plated on a glass coverslip at a density of 1.5×10^5 cells per well in a 24-well plate (ICC) or 1.5×10^6 cells per well in a 6-well plate (Western blot) and cultured at 8.5 % CO_2. Cells were maintained in SATO differentiation medium unless stated otherwise (see Supplementary Table S1 for medium composition). After allowing the cells to attach (1 h), OPCs were treated with vehicle (0.1 % DMSO), the PDE4 inhibitor roflumilast (1 μM, 5 μM or 10 μM) or the PDE4D inhibitor Gebr32a (0.5 μM, 1 μM or 5 μM). Treatment was repeated on day 2 and day 4, applying a 50 % medium change. Cells were fixed with 4 % PFA (ICC) or lysed using RIPA buffer (WB) at day 6 to evaluate OPC differentiation. Importantly, Gebr32a was administered at a non-toxic and non-proliferative concentration (Supplementary Fig S1).

2.3.1.2. Bone marrow derived macrophages

Mouse bone marrow derived macrophages were obtained from 12-week old C57Bl/6J OlaHsd mice and isolated as described previously (Wouters et al., 2012). Briefly, tibial and femoral bone marrow suspensions were plated at a concentration of $10x10^6$ cells/10 cm culture plate. Bone marrow cells were differentiated into macrophages by culturing them in RPMI 1640 medium (Invitrogen), supplemented with 50 U/ml penicillin (Invitrogen), 50U/ml streptomycin (Invitrogen), 10 % heat inactivated fetal calf serum (Gibco) and 15 % L929 conditioned medium.

2.3.1.3. Microglia

Primary microglia were isolated from p0 C57bl6 pups using the shake off method. Meninges-free cerebral cortices were mechanically dissociated and chemically digested using 3U/ml papain to obtain a cell suspension. After 4 days in cultures, culture medium was enriched with 1/3 L929 conditioned medium to generate microglia-enriched glial cultures. Microglia were obtained by using orbital shaking and seeded on a 24-well plate (250.000 cells/well). Microglia were treated with 0.1 % DMSO, 1 μM roflumilast, 1 μM A33 or 1 μM Gebr32a, while simultaneously being stimulated with myelin (100 μg/ml), for 24 h. Next, 10 ng/ml IL-1β (PeproTech) and 100 ng/ml IFN-γ (PeproTech) was added to inflammatory activate microglia. After 24 h, the medium was collected and processes for nitrite assessment using the Griess assay.

2.3.1.4. Brain microvasculature endothelial cells

Murine brain microvascular endothelial cells (BMECs) were isolated from adult 10-week-old mice. After the whole brains were isolated, meninges were removed and cortical tissue was homogenized. Next, the meninges-free brains were digested using a 0.7 mg/ml collagenase and 39 U/ml DNase I mixture for 75 min, followed by a 1 h incubation with a mixture of 1 mg/ml Collagenase/Dispase and 39 U/ml DNase I. Using a 33 % continuous Percoll gradient, the microvessel cells were collected and plated on a Collagen Type IV coated 6-well plate (1brainperwell). After 5 days, BMECs were inflamed using 10 ng/ml TNF-α (PeproTech) and 10 ng/ml IFN-γ (PeproTech) while the treatment with 0.1 % DMSO, 1 μM roflumilast, 1 μM A33 or 1 μM Gebr32a was simultaneously started. After 48 h, cells were processed by means of flow cytometry to evaluate the expression of adhesion molecules.

2.3.1.5. Cerebellar organotypic slice cultures

C57Bl/6J OlaHsd mouse pups (postnatal day 10) were used to generate organotypic cerebellar brain slices. Sagital sections (350 μm) were made from pup cerebellum using a tissue chopper and cultured onto Millicell hydrophilic PTFE cell culture inserts with a pore size of 0.4 μm (Sigma-Aldrich) in a 24-well plate at 3 slices per insert. Media was composed of 50 % minimal essential media (Gibco), 25 % Earle's balanced salt solution (Gibco), 25 % heat inactivated horse serum (Thermo Fisher), 6.5 mg/ml glucose (Sigma-Aldrich), 1 % penicillin–streptomycin (Life technologies) and 1 % glutamax (Thermo Fisher). After allowing a recovery period of 3 days, slices were demyelinated by incubation in lysolecithin (0.5 mg/ml; Sigma-Aldrich) for 16 h. After demyelination, slices were washed in media for 10 min and treatment was initiated 24 h later (vehicle of 0.1 % DMSO, 1 μM roflumilast or 1 μM Gebr32a). Treatment was repeated every other day and continued for 14 days. At the end of the experiment, slices were fixed in 4 % PFA.

2.3.1.6. Microfiber myelination assay

A neuron-free 3D microfiber assay was used to evaluate myelination (Bechler, 2019). Aligned PLLA 2 μm diameter fiber scaffold substrates (AMS.TECL-006-1X; Amsbio) were coated with poly-L-Lysine (PLL) and seeded with murine OPCs, or coated with PLO/laminin and seeded with human iPSC-dervied OPCs, both at a density of 50.000 cells/scaffold (12wellplatecrowninsert) in their respective culture medium described above. One hour after plating, cells were treated with the respective compound. Treatment was repeated every-two days with a 50 % medium change and continued for 14 days. At the end of the experiment, scaffolds were fixed in 4 % PFA.

2.3.1.7. Mapping of OPCs, oligodendrocyte and neurons for isolation from human brain tissue using LCM

Human post-mortem area postrema and chronic inactive MS lesion samples were obtained through the Netherlands Brain Bank (www.bra

inbank.nl) and were sectioned into 10 μm sections on a cryostat (Leica) and mounted on glass cover slides (demographic data in Table 1). Next, neurons (NeuN: 1/200; Millipore MAB377) were stained for in area postrema sections, while oligodendrocytes (GalC: 1/500; Millipore MAB342) and OPCs (NG2: 1/200; Abcam Ab101807) were stained for in MS lesion samples. Briefly, before starting the staining, all containers, jars and working area were rinsed with RNaseZap and nuclease free water (Ambion). Sections were first fixed in ice-cold acetone for 4 min and washed for 5 s in TBS/TBS-T/TBS before endogenous peroxidase was neutralized with 1.5 %H_2O_2 in TBS for 10 s. Next, sections were rinsed with TBS and blocked with 1 %BSA in TBS-T for 10 min. Primary Antibodies were incubated for 30 min followed by a 7-minute horseradish peroxidase (HRP)-linked secondary antibody (vector laboratories) incubation. After rinsing the secondary antibody with TBS, sections were incubated with an avidin-biotinylated horseradish peroxidase complex for 5 min after which visualization of the staining was accomplished using 0.3 % ammonium nickel sulphate and 0.025 % diaminobenzidine (pH 7.8) in TBS. After dehydration (30 s sequential wash in 75 %-95 %-100 % ethanol and 5 min xylene), sections were ready for proceeding to the laser capture microdissection (LCM). Neurons of the area postrema, oligodendrocytes from normal appearing white matter and OPCs from chronic inactive MS lesions were located in the human tissue, isolated using a PALM MicroBeam (Zeiss), and 50 cells per sample per cell type were captured into 0.1-ml tube cap with 10 μl lysis buffer (RNeasy picopure kit, Qiagen).

2.4.1. CRISPR-Cas9

2.4.1.1. Guide RNA design, cloning and transformation

N-terminal specificity between *pde4d* isoforms was defined using NCBI and Ensembl databases. Using the Zhang-lab online webtool (https://crispr.mit.edu), specific single guide RNAs (sgRNAs) were designed against the *N*-terminal of each mouse *pde4d* isoform. For each sgRNA, the lowest off-target prediction was chosen and the frameshift-inducing frequency was determined using the InDelphi algorithm (Shen et al., 2018) (Table 2). The synthesized oligo sgRNAs included an additional guanine nucleotide for increasing its transcriptional efficiency and an overhang to fit into the *Bbs*I restriction gap. Next, 1 μg of plasmid DNA was incubated overnight with 40U *Bbs*I restriction enzyme (Bioké) at 37 °C, which was followed by an enzyme inactivation step were the DNA was incubated at 65 °C for 20 min. After enzyme inactivation, the DNA sample was immediately loaded on a 1 % agarose gel from which the restricted vector was extracted according to the manufacturer's instructions (PCR and gel clean-up kit, Macherey-Nagel, Düren, Germany). A 5:1 insert to vector molar ratio was used to ligate annealed sgRNAs into the linearized vector using T4 DNA Ligase (Bioké) according to the manufacturer's protocol. NEB® 5-alpha competent E. coli cells (Bioké) were used for transforming by means of heathshock and the ligated product and cells were plated on ampicillin (Amp; 100 mg/ml) supplemented LB-agar plates. Single colonies were picked and cultured after overnight propagation, followed by plasmid extraction and purification using a NucleoBond Xtra Midi EF kit (Macherey-Nagel). Correct incorporation of the sgRNA was validated by means of SANGER sequencing.

Table 1
Demographic data of human post-mortem tissue.

Characteristic	Area postrema samples	MS patient samples
Sex (male/female)	4/6	4/6
Age, mean (SD)	78.5 (11.54)	64.7 (9.64)
PMI, mean (SD)	7.288 (2.246)	9.72 (4.09)
Diagnosis (PRMS/SPMS/PPMS/ Unspecified)	n.a.	1/4/3/2

ABBREVIATIONS: MS = multiple sclerosis; SD = standard deviation; PMI = post-mortem interval; PRMS = primary relapsing MS; SPMS = secondary progressive MS; PPMS = primary progressive MS; n.a. = not applicable.

2.4.1.2. Transfection

The pSpCas9(BB)-2A-GFP plasmid was a gift from Feng Zhang (Addgene plasmid #48138; https://n2t.net/addgene:48138; RRID: Addgene_48138). 24 h after seeding, primary mouse OPCs were transfected with the plasmid using the OZ Biosciences NeuroMag Transfection Reagent (Bio-connect). Briefly, 1.75 μl Neuromag reagent was incubated for 20 min (room temperature) with 500 ng plasmid and 50 μl DMEM 6429 medium to allow DNA/Neuromag complex formation. Next, the formed complexes were added dropwise to primary OPC cultures (150 000 cells/well) which were maintained in P/S free SATO medium. The cells were then placed on a magnetic plate in an 8.5 % CO_2 incubator for 30 min to allow magnetofection. After removing the magnetic plate, cells were kept in standard SATO differentiation medium to allow differentiation for a period of six days. The PX458 plasmid (not manipulated) with no target specificity was used as a control.

2.4.1.3. Quantitative qPCR

Total RNA was isolated using the RNeasy mini kit (tissue samples; Qiagen) or the RNeasy picopure kit (laser captured cells; Qiagen) according to the manufacturer's instructions with the use of Qiazol lysis reagent (Qiagen). RNA concentration and purity were determined using a Nanodrop spectrophotometer (Isogen Life science). Consequently, cDNA synthesis was performed using the qScript cDNA SuperMix (Quanta Biosciences). Quantitative PCR was conducted on a StepOnePlus™ Real-Time PCR system (Applied biosystems). The SYBR green master mix (Applied biosystems), 10 μM of forward and reverse primers, nuclease free water and 12.5 ng template cDNA in a total reaction volume of 10 μl. For mouse brain samples, a relative quantification of gene expression was accomplished by using the comparative Ct method with data normalization for to the most stable reference genes. For laser-captured cells, qPCR was performed on paired oligodendrocytes and OPCs and area postrema neurons using verified primer couples for the different *pde4d* splice variants. The proportional contribution of each splice variant was calculated for each sample (sum isoforms per sample = 1). Details of the primers are shown in Table 3.

2.5.1. Nitric oxide (NO) assessment

2.5.1.1. Griess assay

NO was indirectly measured from inflamed mouse monocyte medium (24h, 10 ng/ml IL-1β and 100ng/ml IFN-γ) (PeproTech) using the Griess reagent nitrite measurement kit (Abcam). Briefly, N-(1-naphthyl) ethylenediamine dihydrochloride and sulphanilamide react with the released nitrite present in the culture medium and produce a pink azo dye. Consequently, absorbance of the pink azo dye was measured using a microplate reader (iMark, Bio-Rad) at 540nm.

2.5.1.2. DAF assay

DAF-FM (ab145295) was used to directly detect low concentrations of NO. DAF-FM (5 μM) was added 24 h following inflammatory stimulation. After fixation, cells were mounted on Superfrost Plus glasses to initiate the analysis. Images of immunostainings were acquired using a Digital sight DS-2MBWc fluorescence camera adapted on a Nikon Eclipse 80i microscope. Images (1600 × 1200) were analyzed with ImageJ 1.45e software (NIH; available at: https://rsb.info.nih.gov/ij/). The background was subtracted and the mean fluorescence intensity of the cells was measured for each condition.

2.5.1.3. Western blot

OPC differentiation was determined using MBP-targeted western blot. Total protein content was extracted from treated primary OPC cultures ($1.5x10^6$ cells/well) by homogenization in RIPA buffer (150 mM sodium chloride, 1.0 % Triton X-100, 0.5 % sodium deoxycholate, 0.1 % SDS, 50 mM Tris, pH 8.0) supplemented with a protease (complete Ultra tablets, Roche) and phosphatase (PhosSTOP EASYpack, Roche) inhibitor cocktail. The total protein concentrations were assessed using

Table 2
Oligonucleotide sequences to be annealed and ligated in the PX458 vector as gRNA against PDE4D isoforms.

Isoform	Forward gRNA (5′-3′)	Reverse gRNA (5′-3′)	Frameshift frequency (based on inDelphi algorithm)
pde4d1	CACCGCATCCGAGCATGGCGGGGTA	AAACTACCCCGCCATGCTCGGATG	67.7 %
pde4d3	CACCGTACATGCAACATAGGAGACG	AAACCGTCTCCTATGTTGCATGTAC	89.4 %
pde4d4	CACCGCCCGGGCGGTCAGCGAAGA	AAACTCTTCGCTGACCGCCCGGGC	61.6 %
pde4d5	CACCGAAGTGGATAATCCGCATGT	AAACACATGCGGATTATCCACTTC	61.5 %
pde4d6	CACCGTATTTATTGTCAGTGTCTTG	AAACCAAGACACTGACAATAAATA	80.5 %
pde4d7	CACCGATCTCGTACGGCGACTTTCT	AAACAGAAAGTCGCCGTACGAGAT	85.9 %
pde4d8	CACCGAGAACTAGAACAAGATTGCG	AAACCGCAATCTTGTTCTAGTTCTC	73.7 %
pde4d9	CACCGGTCTACAAGTTCCCTGAGG	AAACCCTCAGGGAACTTGTAGACC	57.5 %

Table 3
Primers sequences.

Gene	Species	Forward primer	Reverse primer
Il-27	*Mus musculus*	CACTCCTGGCAATCGAGATTC	CACTCCTGGCAATCGAGATCC
actb	*Mus musculus*	GGCTGTATTCCCCTCCATCG	CAGTTGGTAACAATGCCATGT
gapdh	*Mus musculus*	ACCACAGTCCATGCCATCAC	TCCACCACCCTGTTGCTGTA
PDE4D1	*Homo sapiens*	AGAACTGAGTCCCCCTTTCC	TGAGCTCCCGATTAAGCATC
PDE4D3	*Homo sapiens*	CCACGATAGCTGCTCAAACA	GTGCCATTGTCCACATCAA
PDE4D4	*Homo sapiens*	TCTGGCGCCTTCAAGTGAG	CAGAGATGCTTGGGGGCTTT
PDE4D5	*Homo sapiens*	TGTTGCAGCATGAGAAGTCC	ATGTATGTGCCACCGTGAAA
PDE4D6	*Homo sapiens*	ATTCGATGGGAAGACGGCTG	CCACAAGCCACGCAGAGTAT
PDE4D7	*Homo sapiens*	GAACATTCAACGACCAACCA	TTCCGGGACATAGACTTTGG
PDE4D8	*Homo sapiens*	CGCACCAGCTCTGACTTCTC	CGCAATCTTGATTTGGCTCT
PDE4D9	*Homo sapiens*	ATGCTGGTTTCCCTTGTGAC	ATGGGCAAGGTTCTAACACG

the Pierce™ BCA Protein Assay Kit (Thermo Fisher Scientific) according to manufacturer's guidelines. Next, 40 μg of protein sample was separated by 10 % sodium dodecyl sulfate polyacrylamide gel electrophorese and blotted onto a PVDF membrane (GE Healthcare, Buckinghamshore, UK). The membrane was transferred into blocking buffer (4 % non-fat dry milk, Tris-buffered saline with 0.1 % Tween-20) for 1 h at room temperature. Primary antibodies were incubated: rat anti-MBP (1/500, MAB386 Millipore) and Mouse anti-β-actin (1/1000, Santa Cruz Biotechnology) for 2 h at room temperature. After washing with TBS-T (Tris-buffered saline with 0.1 % Tween-20) membranes were incubated with secondary antibodies: horseradish peroxidase-conjugated rabbit-anti mouse and goat anti- rat antibodies (Dako, 1:2000) for 1 h at room temperature. An ECL Plus detection kit (Thermo Fisher Scientific) was used and the generated chemiluminescent signal was detected by a luminescent image analyzer (ImageQuant LAS 4000 mini; GE Healthcare).

2.5.1.4. Flow cytometry

The profile of inflammatory cells present in the lymph nodes, spleen or CNS of EAE animals was analyzed by flow cytometry. All analyzed tissues were dissociated into single cells by mashing the tissue through a 70 μm cell strainer. Red blood cells from the spleen were additionally lysed using 0.83 (w/v) ammonium chloride and myelin was removed from CNS samples by using a Percoll gradient. The Zombie NIR Fixable Viability kit (Biolegend, 423105) was used to gate for viable cells. Next, cells were incubated with 10 % rat serum prior to incubating the cells with surface staining antibodies. The Transcription Factor Staining Buffer Set (Thermo Fisher Scientific) was used according to the manufacturer's instructions for fixing and permeabilizing the cells prior to the intracellular staining. Immune cell subtypes were detected using the following antibodies: Pacific Blue anti-mouse CD4 (100427), Brilliant Violet 510 anti-mouse CD8a (100751), FITC anti-mouse CD3 (100203), Brilliant Violet 650 anti-mouse CD19 (115541), Alexa Fluor 700 anti-mouse CD45 (103127), PE/Dazzle 594 anti-mouse IL-17A (506937), PE/Cy7 anti-mouse IFN-γ (505825), PE anti-mouse IL-4 (504103), Alexa Fluor 647 anti-mouse FoxP3 (126407), PerCP/Cy5.5 anti-mouse CD11b (101227) and Brilliant Violet 785 anti-mouse Ly-6c (128041) (all from BioLegend). Samples were acquired using the LSRFortessa (BD Biosciences) and analyzed using FlowJo 10.8.0 (BD Biosciences) (Supplementary Fig S2).

The expression of the adhesion molecules VCAM-1 and ICAM-1 on inflamed BMECs was analyzed using flow cytometry. FVD eFI506 (eBioscience) was used to gate for viable cells. Next, cells were stained for VCAM-1 using a FITC-labeled antibody (Biolegend, 105705) and ICAM-1 using an AF647-labeled antibody (Biolegend, 322718). Both the percentage of positive cells and mean fluorescent intensity was used as a read-out for further analysis.

2.6.1. Immunofluorescence

2.6.1.1. Immunocytochemistry

Organotypic brain slices and both murine and human OPC were fixed in 4 % paraformaldehyde. A 1 % bovine serum albumin (BSA) block was used for 30 min at room temperature. Primary antibodies were incubated for 4 h at room temperature: rat anti-MBP (1:500, MAB386 Millipore), Mouse anti-O4 (1:1000, MAB1326 R&D systems) and/or Rabbit anti-Neurofilament (1:750, Ab8135, Abcam). The glass cover slips, microfiber samples, or MilliPore inserts were then incubated for 1 h in the dark at room temperature with Alexa 488- or Alexa 555-conjugated secondary antibodies (1:600, Invitrogen). Nuclear staining was performed using 4,6′-diamidino-2-phenylindole (DAPI; Invitrogen) for 10 min. The glass cover slides, microfiber samples and organotypic brain slice membranes were mounted onto cover glasses with Fluoromount-G. OPC differentiation analysis using the Leica DM2000 LED microscope (20x magnification pictures; 5 random pictures per cover slide) and Fiji, ImageJ (manual threshold of MBP and O4 positive area corrected for the number of cells per picture). The microfiber and organotypic brain slices samples were imaged under a Zeiss LSM880 confocal microscope (0.42 μm z-steps with a 40x/1.1 water objective). The number of complete myelin sheaths, and the average and complete length of complete myelin sheaths per cell were determined in the microfiber myelination assay. The myelination index was calculated for the brain slice experiment, which is the volume of MBP and neurofilament colocalization corrected for the area of neurofilament present per z-layer. 3D rendering images were made afterwards using the VAA3D software (VAA3D-Neuron2_Autotracing) (Peng et al., 2014).

2.6.1.2. Immunohistochemistry

Frozen coronal brain sections (bregma −2mm; 10 μm; cuprizone study) and both transversal and longitudinal spinal cord sections (10 μm; EAE study) were generated via cryosectioning (Leica) and were stained for MBP or F4/80 and Arginase respectively. Briefly, sections were air-dried and fixed in acetone for 10 min. Non-specific binding was blocked using 10 % DAKO protein block in PBS for 1 h. Cuprizone brain sections were incubated overnight with rat anti-MBP (1:500, MAB386 Millipore) or anti-CC1 (1:50) (Calbiochem), longitudinal spinal cord sections with both rat anti-F4/80 (1:100, MCA497G, Serotec) and mouse anti-arginase 1 (1:100, 610708, BD Trasnduction lab), and transversal spinal cord sections with both rat anti-MBP (1:500, MAB386 Millipore) and rabbit-anti neurofilament (1:750, Ab8135, Abcam) at 4 °C. Next, after three washing steps with PBS, sections were incubated with Alexa 488- or Alexa 555-conjuagted secondary antibodies (1:600, Invitrogen) for 1 h. Nuclei were counterstained with DAPI and coverslips were mounted using fluorescent mounting medium (DAKO). For the cuprizone experiment, 3 images per animal per region (corpus callosum and dentate gyrus) were collected (between anterior posterior coordinates −1.5 mm and −1.9 mm relative to Bregma). For the EAE experiment, 5 random images within each longitudinal spinal cord section (3sectionsperanimal) were taken, thereby comprising the cervical, thoracal and lumbar spinal cord regions. The cervical spinal cord region was used for generating transversal sections and 3 random images per section were collected (5sectionsperanimal). Images were taken using the Leica DM2000 LED microscope and quantified with Fiji, ImageJ. MBP quantification was performed in a blinded manner and was based on the area percentage positive for MBP in the corpus callosum by means of a manual threshold adjustment. For the spinal cord sections, the double positive area for F4/80 and Arginase 1 was determined using the colocalization plugin of Fiji, ImageJ. The results obtained were averaged to obtain one representative value per animal.

2.6.1.3. Transmission electron microscopy

The sample preparation for TEM was performed as described previously (Maheshwari et al., 2013) with minor modifications. For the corpus callosum analysis of the cupizone studies, a coronal brain block (1mmthick) within the anteroposterior coordinates from −0.3 to −1.5 mm was cut in the midsagittal plane. For assessing remyelination in the EAE model, the optic nerve was isolated. The collected tissues were fixed with 2 % glutaraldehyde and post-fixated with 2 % osmiumtetroxide in 0.05 M sodium cacodylate buffer (pH = 7.3) for 1 h at 4 °C. Tissues were then stained with 2 % uranyl acetate in 10 % acetone for 20 min, dehydrated through graded concentrations of acetone and embedded in epoxy resin (araldite). Semithin sections (0.5 μm) were stained with a solution of thionin and methylene blue (0.1 % aqueous solution) for light microscopic examination to delineate the region of interest. Subsequently, ultrathin sections (0.06 μm) were cut and mounted on 0.7 % formvar-coated grids and contrasted with uranyl-acetate followed by lead citrate and examined on a Philips EM 208 transmission electron microscope (Philips, Eindhoven, The Netherlands) operated at 80 kV.2.9. G ratios (=diameter axon/diameter axon with myelin sheath) were measured to evaluate myelin thickness using Fiji, Image J.

2.7.1. Emesis indicators

2.7.1.1. Patch clamp

Acute coronal brain slices were made from 12 to 16 week old male C57Bl6 mice using a Leica vibratome. Putative area postrema neurons were identified based on location relative to the central canal and electrophysiological characteristics. Pipettes of 4–6 MOhm resistance filled with a Na HEPES-based solution were used for extracellular recordings using the loose cell attached method as described by (Branch and Beckstead, 2012). Baseline firing rate was recorded for four minutes, after which either Gebr-32a or roflumilast (blinded) was bath perfused for six minutes.

2.7.1.2. Xylazine/ketamine anesthesia test

The duration of anesthesia induced by the combination of xylazine (10 mg/kg i.p) and ketamine (60 mg/kg i.p) was determined in C57Bl6 mice. Fifteen minutes following the induction of anesthesia, mice were treated with different doses of A33, Gebr32a or roflumilast. The duration of anesthesia was assessed by the return of the righting reflex (Nelissen et al., 2019).

2.7.1.3. Statistical analysis

GraphPad Prism 9.0.0 software (GraphPad software Inc) was used to perform statistical analyses. The sample size of each experiment was determined using G*Power based power analysis. Outlier values were determined based on the Dixon test for extreme values (significance level of 0.05) and excluded for further analysis. Differences between groups were evaluated using a non-parametric Kruskal-Wallis test with Dunn's post-hoc analysis against the vehicle group when the sample size was $n \leq 5$. When the sample size was $n \geq 6$, normality was checked using the Shapiro-Wilk test for normality. Normally distributed data were subsequently analyzed with a one-way ANOVA with Tukey's (*in vivo* and post-mortem analysis) or Dunnett's (*in vitro* editing experiment) multiple comparison. Differences between EAE scores were evaluated using a non-parametric Friedman test with Dunn multiple comparison against vehicle group. Subsequently, differences of the AUC calculated from EAE scores over time were evaluated using a non-parametric Kruskal-Wallis test with Dunn's post-hoc analysis against the vehicle. Differences over time within the VEP experiment were evaluated using a repeated measure two-way ANOVA with Šídák's multiple comparisons test. Behavioural experiments were evaluated for differences compared to chance level using one-sample *t* test. All data are displayed as mean ± SEM, *P ≤ 0.05, **P ≤ 0.001, P ≤ 0.005, #P ≤ 0.05, ##P ≤ 0.01.

3. Results

3.1. PDE4D inhibition stimulates OPC differentiation and enhances remyelination in cerebellar organotypic brain slices

To decipher the myelin-promoting effects of PDE4 (roflumilast), PDE4B (A33) and PDE4D (Gebr32a) inhibition, we treated primary mouse OPCs with either one of the inhibitors at different concentrations to subsequently evaluate cellular differentiation. By analyzing the number of myelin basic protein (MBP) positive cells to assess OPC differentiation, together with the $O4^+$ area (pre-mature oligodendrocyte marker) and MBP^+ area (terminally differentiated oligodendrocyte marker), we demonstrated an increase of OPC maturation upon 6 days of 1 μM roflumilast (Kruskal-Wallis test with Dunn's post-hoc analysis; $F(3,12) = 10.70$;**P ≤ 0.01) (Fig. 1A-D) or either 1 μM or 5 μM Gebr32a treatment (Kruskal-Wallis test with Dunn's post-hoc analysis; $F(3,18) = 17.77$;**P ≤ 0.01) (Fig. 1E–H). Differentiated oligodendrocytes show clear morphological complexity and extensive process formation, which precedes axonal ensheathment. Furthermore, total MBP levels were measured by Western blotting and confirmed the immunocytochemical observations of increased MBP protein levels upon PDE4/PDE4D inhibition (two-tailed Mann-Whitney test, *P ≤ 0.05) (Fig. 1I and J). Importantly, A33-induced PDE4B inhibition did not enhance OPC differentiation (Fig. 1K and L). Furthermore, similar morphological complexities were observed when culturing primary OPCs on the differentiation inhibiting coating fibronectin (Fig. 2A–C).

To assess the role of PDE4/PDE4D inhibition on myelination and remyelination, we made use of electrospun microfibers and organotypic cerebellar brain slice cultures as they both are able to demonstrate myelination along definable fibers or axons respectively. We found that PDE4 and PDE4D inhibition led to significantly more longer and complete myelin sheaths per oligodendrocyte in both murine-derived primary oligodendrocytes (Kruskal-Wallis test with Dunn's post-hoc analysis; $F(2,18) = 10.78$; $F(2,18) = 11.52$; $F(2,18) = 14.03$; *P ≤ 0.05; **P ≤ 0.01; ***P ≤ 0.005) (Fig. 3A-D) or human iPSC-derived

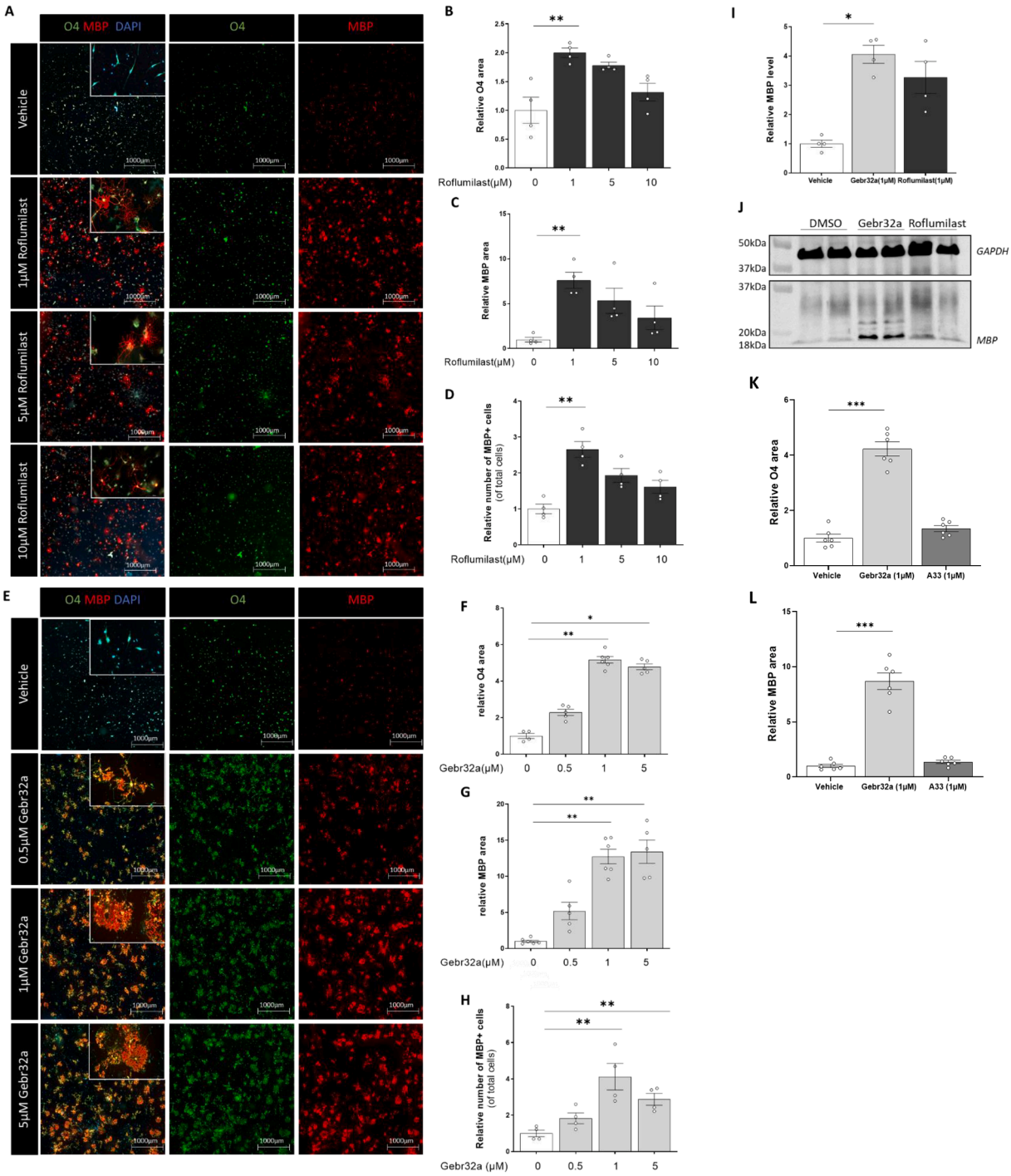

Fig. 1. Inhibition of PDE4D by Gebr32a induces OPC differentiation, while PDE4B inhibition by A33 does not alter OPC differentiation. Primary mouse OPCs were allowed to differentiate for 6 days and were treated on day 0, 2 and 4 with different concentrations of (A) roflumilast (1 μM, 5 μM, 10 μM) or (D) Gebr32a (0.5 μM, 1 μM, 5 μM) or A33 (1 μM). After 6 days of culture, cells were stained for O4 (late OPC marker) and MBP (oligodendrocyte marker). (D and H) The number of MBP^+ cells, (B, F and K) $O4^+$ area and (C, G and L) MBP^+ area was measured and corrected for the amount of cells ($n \geq 4$/group) (I-J) The total level of MBP and β-actin protein expression upon roflumilast (1 μM) or Gebr32a (1 μM) treatment was determined by means of western blotting and the ratio of MBP to β-actin is displayed ($n = 4$/group). The sample size 'n' represents the number of wells obtained from minimally-three independent cell culture experiments. Data were analyzed using a non-parametric Kruskal-Wallis test with Dunn's multiple comparisons. Data are displayed as mean +/-SEM. (*p ≤ 0,05; **p ≤ 0,001; ***p ≤ 0,005).

oligodendrocytes (Kruskal-Wallis test with Dunn's post-hoc analysis; $F(2,15) = 11.61$; $F(2,15) = 10.86$; $F(2,15) = 12.07$; *$P \leq 0.05$; **$P \leq 0.01$) (Fig. 3E–H). Brain slice cultures were demyelinated by means of lysophosphatidylcholine (LPC) and remyelination was allowed for 14 days with or without a PDE4 or PDE4D inhibitor. Kruskal-Wallis analysis of the slice cultures at the end of the experiment showed a clear increase in axonal myelin ensheathment upon PDE4D inhibition compared to vehicle treated slices (Dunn's multiple comparison analysis, $F(2,15) = 15.16$; *$P \leq 0.05$) (Fig. 3I-J).

3.2. PDE4D inhibition enhances remyelination, and thereby promotes functional recovery, after cuprizone-induced demyelination

The effect of PDE4/PDE4D inhibition on remyelination was further

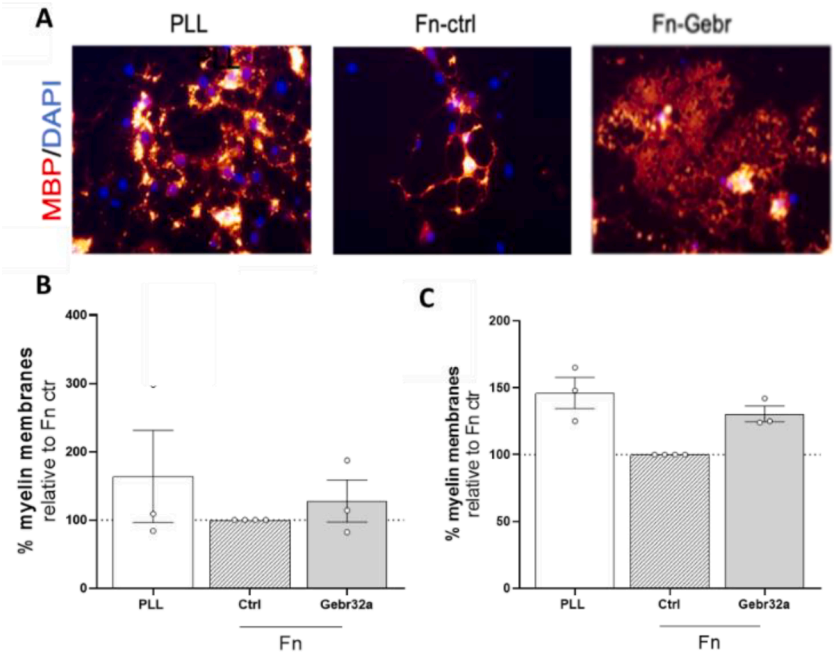

Fig. 2. Exposure to PDE4D-inhibitor Gebr32a overcomes inhibition of myelin membrane formation by fibronectin. (A) Representative images of MBP immunocytochemistry of OPCs treated from day 3 onwards. (B and C) Quantitative analysis of the percentage of MBP-positive cells and the percentage of MBP-positive oligodendrocytes (OLGs) bearing myelin membranes treated from day 3 onwards. Each bar represents the mean ± SEM of the relative percentages of 3 independent experiments. In each independent experiment, the percentages of untreated cells grown on a Fn substrate were set at 100 % (horizontal line, black bar). Exposure to Gebr32a at day 3 of differentiation overcomes Fn-mediated inhibition (compared to positive control PLL) of myelin membrane formation in primary oligodendrocyte monocultures. No statistical analysis was conducted due to the low sample size.

examined *in vivo* using the acute cuprizone model (0.3 % w/w for 6 weeks). After cuprizone administration, animals were returned to a normal chow diet to allow spontaneous remyelination (Fig. 4A). At the end of the demyelination period, spatial memory assessment in the OLT demonstrated an impairment upon cuprizone intoxication (two-tailed one sample *t*-test against d2 $\neq$ 0;** P < 0.01; *** P < 0.005) (Supplementary Fig S3). To make sure sufficient compound concentrations accumulated in the brain to immediately initiate remyelination, we started the treatment regimen two days before ceasing the cuprizone diet. Following cuprizone withdrawal and upon treatment during the remyelination period, the roflumilast-treated group (3 mg/kg, s.c.) and the Gebr32a-treated group (0.3 mg/kg, s.c.) showed recovery of spatial memory performances (two-tailed one sample *t*-test against d2 $\neq$ 0; *P < 0.05; ***P < 0.005) (One-way ANOVA with Tukey's multiple comparisons; F (3,74)= 4.894; #P $\leq$ 0.05; ##P $\leq$ 0.01) (Fig. 4B and C). As VEP latency time is correlated with optic nerve de- and remyelination, we implemented epidermal flash VEP measurements (3 trains of 20 stimuli, 10 μs duration, 1 Hz frequency) of both eyes during both de- and remyelination (Marenna et al., 2022). Significantly increased latency times were observed at the end of cuprizone administration indicating demyelination of the optic nerve, and they were significantly decreased upon PDE4D inhibition during remyelination, indicating functional remyelination (repeated measure two-way ANOVA with Sidak's multiple comparison test; F (2,18)= 63.27; **P $\leq$ 0.01; ***P $\leq$ 0.005) (Fig. 4D). Post-mortem analysis revealed a significantly increased MBP$^+$ area upon PDE4 or PDE4D inhibition in both the corpus callosum and hippocampal dentate gyrus after 10 days of treatment (One-way ANOVA with Tukey's multiple comparisons, F (3,33)= 15.34; F (3,31)= 36.15; F (3,32)= 6.281; F (3,32)= 5.743; *P $\leq$ 0.05; **P $\leq$ 0.01; ***P $\leq$ 0.005) (Fig. 4E-J). This increase in MBP$^+$ area was accompanied with an increased number of CC1 + oligodendrocytes in the corpus callosum (Kruskal-Wallis test with Dunn's multiple comparison; F(3,20) = 14.52; ***P $\leq$ 0.005) (Fig. 4K-L). In line, PDE4 and PDE4D inhibition during remyelination significantly decreased the G ratios in the corpus callosum (Kruskal-Wallis test with Dunn's multiple comparison; F(3,26) = 13.19; F(3,16) = 12.90) and increased the number of myelinated axons (Kruskal-Wallis test with Dunn's multiple comparison; F(3,26) = 15.38; F(3,16) = 13.26) (*P $\leq$ 0.05; **P $\leq$ 0.01) (Fig. 3M-T). Collectively, these results show that PDE4D inhibition establishes functional remyelination in the acute cuprizone model.

3.3. PDE4D isoforms show distinct expression patterns indicative for their functional contribution

Next, we determined the different *PDE4D* isoform expression profiles in laser capture micro-dissected neurons of the human area postrema, the primary CNS area involved in emesis. We showed a particularly high mRNA expression of the long *PDE4D7* isoform in these neurons, while *PDE4D1/2, PDE4D4* and *PDE4D6* were very lowly expressed (Fig. 5A and 5B). Interestingly, when comparing these expression profiles to laser capture micro-dissected OPCs derived from chronic inactive human MS lesions, abundantly present in progressive MS stages, and NAWM oligodendrocytes, we saw a clear distinction between isoform expressions (Fig. 5A and 5B). Especially *PDE4D6*, and to a lesser extent *PDE4D1/2* expression levels were more abundantly present in OPCs and to a lesser extent in oligodendrocytes. As no isoform-specific PDE4D inhibitors exist, and we aimed to validate the role of the different PDE4D isoforms in OPC differentiation, we made use of a CRISPR-Cas9 system to specifically knock down selected isoforms. Guide RNAs were designed to the *N*-terminus of each unique PDE4D isoform specifically. In this way, an in/del can be created at the targeted location, creating a frameshift and therefore a non-functional enzyme. Six days post-transfection (transfection efficiency of 55 %), a higher number of primary mouse OPCs transfected with either *pde4d1/2* or *pde4d6* targeting CRISPR/Cas9 plasmids was MBP$^+$, indicating an induction of OPC differentiation (One-way ANOVA with Dunnett's multiple comparison; F(8,36) = 64.56; ***P $\leq$ 0.005) (Fig. 5C and 5D). These data indicate that the short PDE4D1 and PDE4D6 isoforms might skew differentiation in OPCs, while their expression is mostly lacking in neurons in the area postrema, which are responsible for emesis.

3.4. The PDE4B inhibitor A33 diminishes neuro-inflammation, while the PDE4D inhibitor Gebr32a increased CNS myelin content in EAE

To understand whether PDE4D and PDE4B inhibition shows differential effects on neuroinflammation versus myelination, we studied the therapeutic potential of the pan PDE4 inhibitor roflumilast, the PDE4B inhibitor A33 and the PDE4D inhibitor Gebr32a in the chronic EAE model. During the early acute phase of the model, neuroinflammation is prominent, while the level of myelination can be studied during the chronic phase of the disease. Therefore, as a readout, we assessed

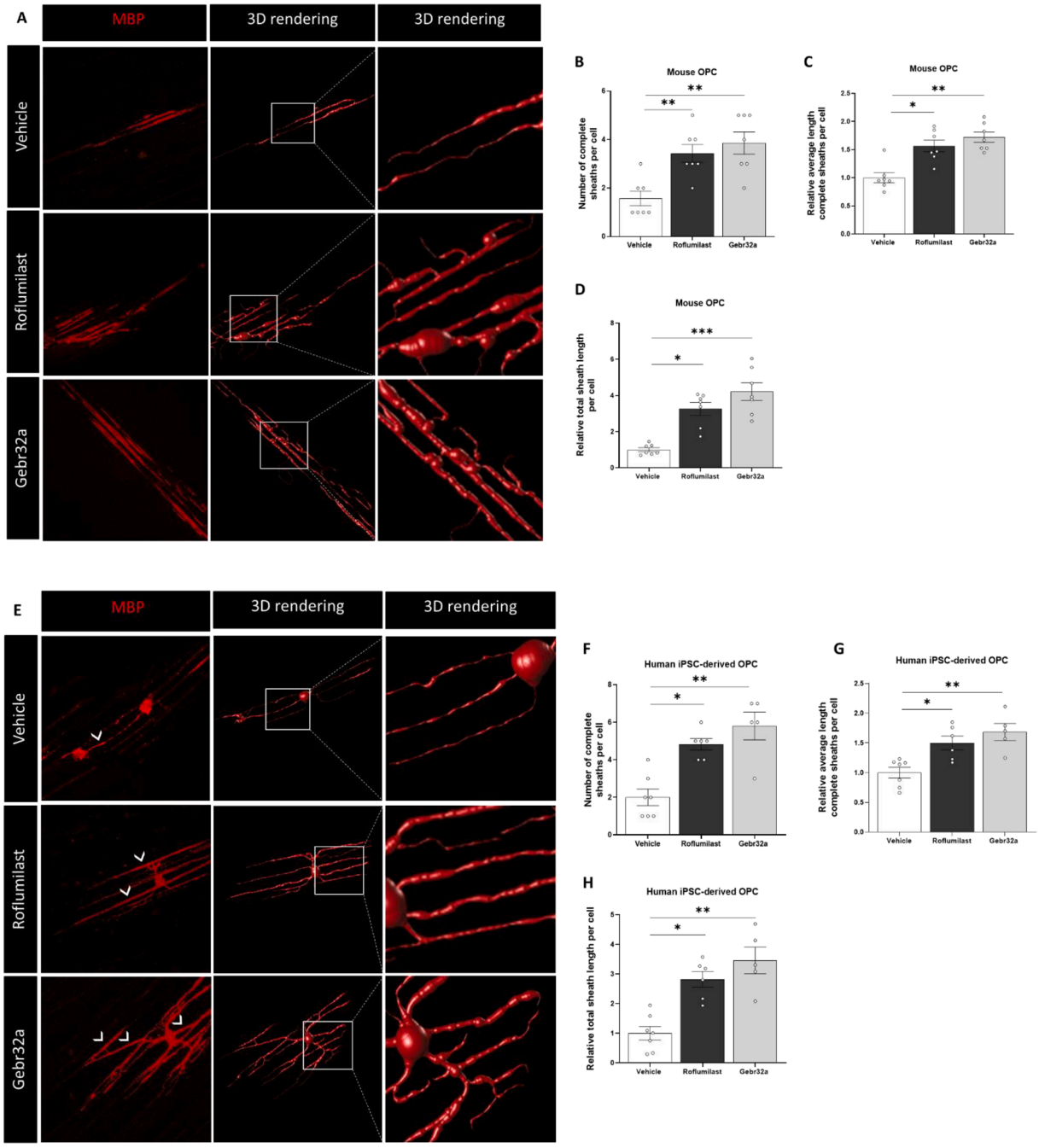

Fig. 3. Inhibition of PDE4D by Gebr32a increases (re)myelination of mouse OPCs, human iPSC-derived OPCs, and organotypic brain slices. Confocal and 3D rendered images showing the formation of myelin-like extensions on microfibers by (A) primary mouse OPCs and (E) human iPSC-derived OPCs. Quantitative data analysis shows a higher number of complete myelin sheath formation, an increased average length of the formed complete myelin sheaths, and an increased total length of complete myelin sheaths per cell upon 1 μM roflumilast or 1 μM Gebr32a treatment of both (B-D) primary mouse OPCs and (F-H) iPSC-derived OPCs ($n \geq 5$/group). (I-J)). Mouse brain slices (350 μM) were demyelinated using lysolecithin (16 h) and subsequently treated for 14 days with vehicle (0,1%DMSO), 1 μM roflumilast or 1 μM Gebr32a. After 14 days of remyelination, slice cultures were stained for MBP and neurofilament. The relative myelination index is determined on the level of MBP and neurofilament co-localization, corrected for the amount of neurofilament positive axons ($n = 6$/group). For the microfiber myelination assay, the sample size 'n' represents the number of wells obtained from minimally-three independent cell culture experiments (mouse OPCs) or from three iPSC-derived differentiations in which minimally 5 cells per insert were quantified and averaged. For the brain slice experiment, the sample size 'n' represents the number of inserts obtained from minimally-three independent brain slice isolations. Data were analyzed using a non-parametric Kruskal-Wallis test with Dunn's multiple comparisons. Data are displayed as mean +/-SEM (*$p \leq 0{,}05$; **$p \leq 0{,}001$; ***$p \leq 0{,}005$).

clinical scores, cognitive performance pre-onset of neurological symptoms, immune cell phenotype, and the level of de- and remyelination of the animals.

At four and ten days after EAE induction, pre-onset of the clinical symptoms, spatial memory was assessed in the OLT and the average performance was taken for further analysis. Mice treated with roflumilast (3 mg/kg) or A33 (3 mg/kg) displayed intact spatial memory (two-tailed one sample *t*-test against d2 $\neq$ 0; ** $P \leq 0.01$; *** $P \leq 0.005$)

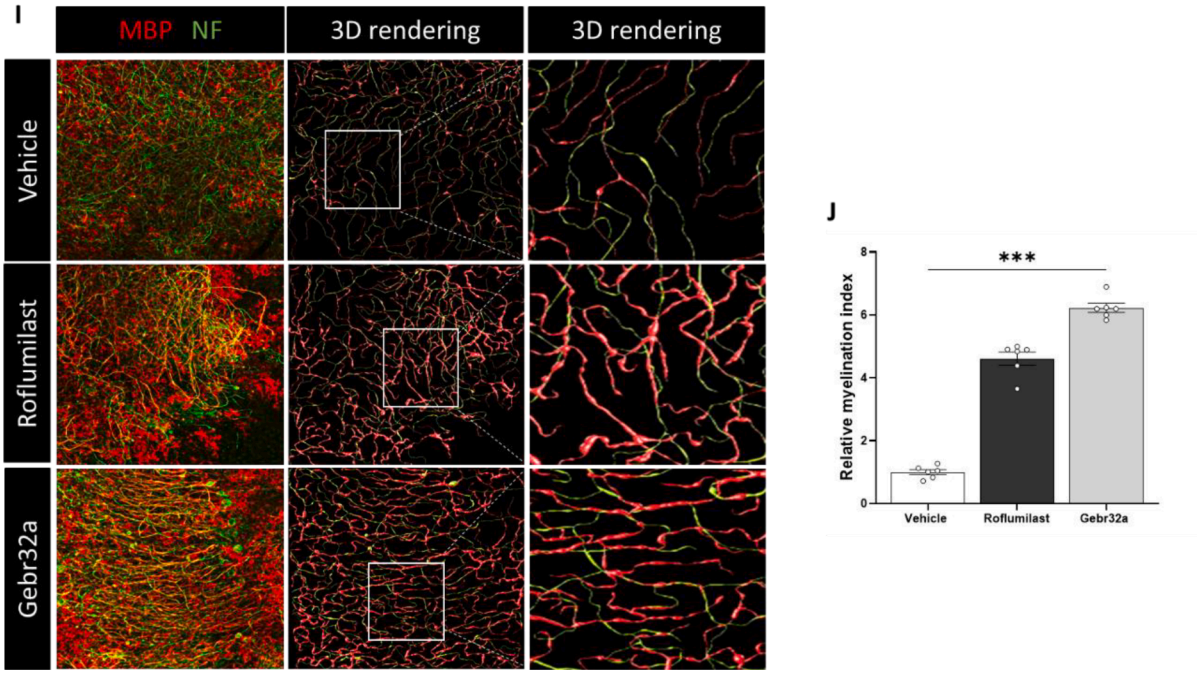

Fig. 3. (*continued*).

whereas the vehicle and Gebr32a-treated groups displayed impaired spatial memory following induction of the EAE (Fig. 6A). In line with this, roflumilast and A33 suppressed EAE clinical scores (area under curve; AUC) during the inflammatory phase of the disease from (Friedman test with Dunn's multiple comparison $F(3,59) = 64.44$; ***$P \leq 0.005$) (non-parametric Kruskal-Wallis test with Dunn's post-hoc analysis for AUC). In contrast, Gebr32a (3 mg/kg) did not affect the neurological disabilities in this phase (Fig. 6B). During a 10-day washout period (d34 - d44 d.p.i.), clinical symptoms increased in roflumilast and A33-treated groups. Restarting the treatment regimen in the chronic stage of EAE at 45 days post induction showed a reversal in efficacy of the inhibitors. While roflumilast and Gebr32a significantly reduced clinical symptoms, A33 was no longer effective at this chronic stage of the disease (Friedman test with Dunn's multiple comparisons; $F(3,20) = 29.17$; *$P \leq 0.05$, ***$P \leq 0.005$) (non-parametric Kruskal-Wallis test with Dunn's post-hoc analysis for AUC) (Fig. 6B).

Flow cytometry was performed at peak of the disease (day 20p.i.) and at the end of the chronic stage (day 65p.i.)(Supplementary Fig S2). At peak, the CNS of the A33 and roflumilast treated-animals exhibited a reduced percentage of pathogenic T cells ($CD45^+CD3^+CD4^+IFN\gamma^+$) (non-parametric Kruskal-Wallis test with Dunn's post-hoc analysis; $F(3,16) = 10.67$; *$P \leq 0.05$), and a relative increase of non-pathogenic T cells ($CD45^+CD3^+CD4^+IFN\gamma^-IL17^-$) (non-parametric Kruskal-Wallis test with Dunn's post-hoc analysis; $F(3,16) = 10.24$; *$P \leq 0.05$), whereas no differences were noted at the end stage (day 65p.i.) (Fig. 6C-I). A non-parametric Kruskal-Wallis test revealed a significant reduction of inflammatory monocytes ($CD45^+CD11^+Ly6c^{High}$) (Dunn's post-hoc analysis; $F(3,16) = 14.79$;**$P \leq 0.01$) and an increased *Il-27* mRNA expression in the brain (Dunn's post-hoc analysis; $F(3,13) = 12.26$; *$P \leq 0.05$**$P \leq 0.01$) of A33 and roflumilast, but not Gebr32 treated animals (Fig. 6J). No differences in regulatory T cells were observed, nor at peak or at the end of the experiment (Supplementary Fig S4). Additionally, the spinal cord of roflumilast or A33 treated animals showed an increased presence of $Arginase^+$ infiltrated monocytes, indicating a shift towards $Arg1^+$ macrophages (Kruskal-Wallis test; Dunn's post hoc analysis; $F(3,16) = 14.79$; *$P \leq 0.05$; **$P \leq 0.01$) (Fig. 6K and L). The total number of infiltrating lymphocytes or monocytes did not differ over the complete EAE disease course (Supplementary Fig S5), nor were any differences detected in peripheral tissues including lymph nodes and spleen in any of the treatment groups. At the end of the disease course, an MBP staining on transversal sections of the spinal cord of these animals displayed a significantly increased MBP^+ area upon roflumilast and Gebr32a, but not upon A33 treatment (non-parametric Kruskal-Wallis test with Dunn's multiple comparisons; $F(3,16) = 16.71$; *$P \leq 0.05$; ***$P \leq 0.005$) (Fig. 6M and N). Ultrastructural myelin imaging using TEM confirmed the immunohistochemical observations displaying decreased G ratios and an increased number of myelinated axons in the optic nerve of the animals treated with roflumilast and Gebr32a treatment, but not when treated with A33 (day 65 d.p.i.) (non-parametric Kruskal-Wallis test with Dunn's multiple comparisons; $F(3,16) = 15.34$; *$P \leq 0.05$; **$P \leq 0.01$) (Fig. 6O-R). These data indicate an increase in myelin content during the chronic stage of the disease.

3.5. *pde4b*$^{-/-}$ bone marrow transplantation promotes clinical recovery in EAE by diminishing neuro-inflammation

Since pharmacological inhibition of PDE4B by means of A33 diminished neuro-inflammation, we next aimed to further determine the involvement of Pde4b during EAE disease course by performing a bone-marrow transplantation of *pde4b*$^{-/-}$, *pde4b*$^{+/-}$, *and pde4b*$^{+/+}$ mice into lethally irradiated wild type acceptor mice preceding EAE induction (Fig. 7A). The onset of the disease (day 10p.i.) was not affected, but, based on a non-parametric Kruskal-Wallis test, knockout *pde4b*$^{-/-}$ and *pde4b*$^{+/-}$ heterozygous bone marrow receivers displayed a significant gene dose-dependent reduction in the clinical scores (Tukey's multiple comparison test, $F(2,27) = 12.73$; ***$P \leq 0.005$) (Fig. 7B-C). In line with pharmacological PDE4B inhibition, the CNS at disease peak of *pde4b*$^{-/-}$ bone marrow receivers showed an increased percentage of anti-inflammatory or patrolling phagocytes ($CD45^+CD11^+Ly6c^{low}$) (Kruskal-Wallis test with Dunn's multiple comparisons; $F(2,12) = 9.454$; *$P \leq 0.05$) and non-pathogenic T lymphocytes ($CD45^+CD3^+CD4^+IFN\gamma^-IL17^-$) (Kruskal-Wallis test with Dunn's multiple comparisons; $F(2,12) = 10.66$; **$P \leq 0.01$), while inflammatory monocytes ($CD45^+CD11^+Ly6c^{High}$) (Kruskal-Wallis test with Dunn's multiple comparisons; $F(2,12) = 8.637$; **$P \leq 0.01$) and pathogenic T lymphocytes ($CD45^+CD3^+CD4^+IFN\gamma^+$) were significantly decreased (Fig. 7D-G).

To study whether PDE4B inhibition directly skews the phagocyte phenotype shift, thereby affecting the inflammatory activity, both

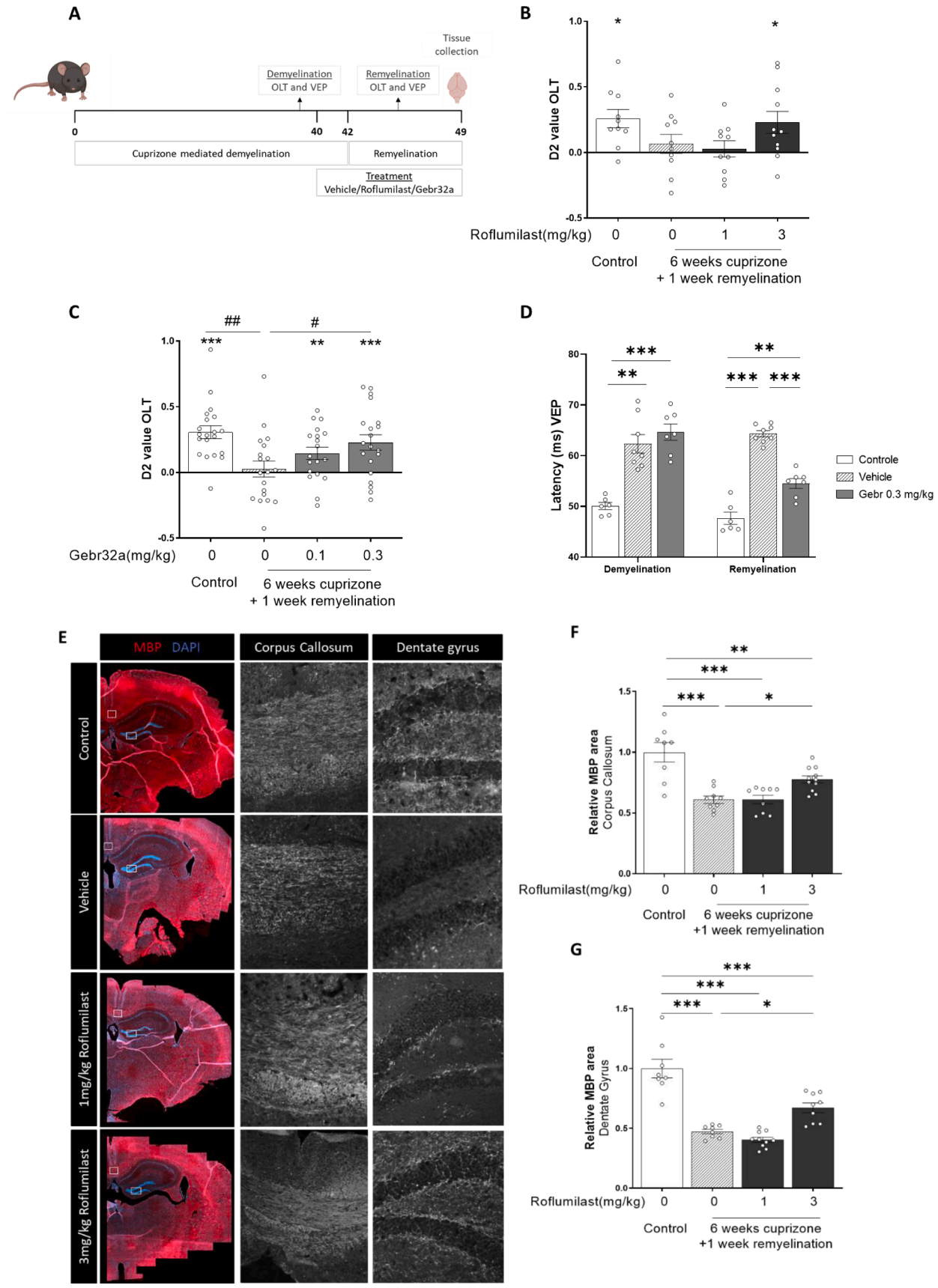

Fig. 4. Inhibition of PDE4D by Gebr32a improves functional remyelination, as measured by means of the spatial memory performances and visual evoked potential latency times. (A) Schematic representation of the cuprizone experiment. (B-D) Functional remyelination was evaluated by means of the OLT at the 3 h inter-trial-interval to evaluate spatial memory performances, and while visual evoked potential latency times were determined to assess optic tract and central nervous system signaling (n ≥ 6/group). At the end of the experiment, all animals were sacrificed and brains were isolated. At anteroposterior coordinates from −0.3 to −1.5 mm

(midsagittal slice), the brain was used for TEM analysis. The remaining posterior part of the brain was used for slicing and immunohistochemistry against MBP. (E and H) Representative pictures of MBP staining in the corpus callosum and dentate gyrus. The MBP + area in both the (F and I) corpus callosum and (G and J) dentate gyrus of the hippocampus were analyzed ($n \geq 8$/group). (K-L) While cuprizone diet reduced the number of oligodendrocytes in the corpus callosum, 3 mg/kg roflumilast and 0.3 mg/kg Gebr32a treatment caused a robust increase in CC1 + oligodendrocytes ($n = 5$/group). (K-P) G ratios and the amount of myelinated axons were measured based on corpus callosum TEM pictures ($n \geq 4$/group). A one sample *t*-test was performed to test for spatial memory (e.g. $D2 \neq 0$). A one-way ANOVA with Tukey's multiple comparison test was performed to evaluate significances among groups in the OLT (#$p < 0{,}05$; ##$p < 0{,}01$). A two-way ANOVA with Sidak's multiple comparison test was performed to test for significances in the VEP latency times. MBP + area differences were analyzed with a one-way ANOVA with Tukey's multiple comparison test. Significant differences for the amount of $CC1^+$ cells, G ratio measurements and percentage of myelinated axons were evaluated with a non-parametric Kruskal-Wallis test with Dunn's multiple comparisons. Data are displayed as mean +/-SEM (*$p < 0.05$; **$p < 0.01$; ***$p < 0.005$).

murine BMDMs and microglia were exposed to mouse myelin (48 h) and an inflammatory trigger (IFNγ and IL-1β; 24 h). We observed that PDE4B inhibition by 1 μM A33 significantly suppressed the murine phagocytic nitrite release in the medium, which is an indicator of nitric oxide production (Kruskal-Wallis test with Dunn's multiple comparisons; $F(3,16) = 16.28$; $F(3,21)$; *$P \leq 0.05$)(Fig. 8A and B). Furthermore, ICAM-1 and VCAM-1 adhesion molecule levels were measured on primary brain microvasculature endothelial cells (BMEC) using flow cytometry. Following PDE4 or PDE4B inhibition, mean fluorescent intensity levels of ICAM-1 were significantly reduced indicating a reduced ICAM-1 protein abundance (Kruskal-Wallis test with Dunn's multiple comparisons; $F(3,23) = 9.388$;*$P \leq 0.05$) (Fig. 8C-F).

To evaluate whether PDE4B inhibition is also able to skew the human macrophage phenotype shift, human MDMs were exposed to human myelin (48 h) and an inflammatory trigger (IFNγ and IL-1β; 24 h). A33 attenuated the NO production in human macrophages, as measured by a decrease in DAF fluorescent signal (Kruskal-Wallis test with Dunn's multiple comparisons; $F(3,20) = 18.22$;*$P \leq 0.05$; ***$P \leq 0.005$) (Fig. 8G and 8H). These findings, together with the *in vivo* immunomodulatory actions, position PDE4B as an important target for reducing the neuroinflammatory status in MS.

3.6. The therapeutic dose of Gebr32a and A33 is not accompanied with emetic-like side effects

Given the emetic potential pan PDE4 inhibitors possess, the duration of the xylazine/ketamine α2-adrenergic receptor-mediated anesthesia was measured upon roflumilast, Gebr32a or A33 treatment (Fig. 9A). While the known emetic dosage of roflumilast (3 mg/kg, s.c.) significantly reduced the anesthesia duration, neither tested concentration of A33 or Gebr32a altered the time until the righting reflex compared with the vehicle condition (non-parametric Kruskal-Wallis test with Dunn's post-hoc analysis; $F(14,131) = 52.79$; **$P \leq 0.01$). In line with this finding, only 1 μM of roflumilast bath perfusion increased electrical activity in neurons of the murine area postrema while this effect was not observed for 1 μM Gebr32a (Fig. 9B).

4. Discussion

Targeting the destructive immunological interplay in MS and promoting endogenous remyelination are key goals in developing novel MS therapeutics. In line with previous studies, we confirmed that full PDE4 inhibition by means of roflumilast supports neuro-regenerative responses and suppresses neuroinflammation in different animal models of MS (32, 35, 72–75). Next, we segregated the myelination-promoting role of PDE4 inhibition into a PDE4D-dependent process, while selective PDE4B inhibition accounted for the anti-inflammatory effects. However, the major drawback in translating PDE4 inhibitors towards clinical applications are the predicted emetic side effects ascribed to *PDE4D* expression in the *area postrema* in the medulla oblongata (50). Interestingly, we show here for the first time that short and super-short *PDE4D* isoforms are hardly expressed in the neurons of human *area postrema*, while highly expressed in human OPCs. These findings render the (super-)short PDE4D isoforms an interesting target to safely enhance remyelination. Therefore, by selectively and complementary inhibiting PDE4 genes, we provide a new opportunity to enhance remyelination without triggering the emetic side effects linked to full PDE4 inhibition.

In our study, we identified that PDE4D inhibition in particular is sufficient to stimulate OPC differentiation by inducing MBP protein levels in primary OPCs, both on PLL coated substrate as well as in the presence of fibronectin. Both primary murine OPCs and human iPSC-derived OPCs significantly increased their number and length of myelin sheaths surrounding electro-spun microfibers upon PDE4D inhibition. Consequently, in an *ex vivo* cerebellar brain slice model, PDE4D inhibition increased the level of remyelination after LPC-induced demyelination. The enhanced differentiation of OPCs and the consecutive induction of (re)myelination upon roflumilast treatment is consistent with previous studies reporting beneficial effects of both cAMP analogous (e.g. dibutyryl cAMP and 8-bromo cAMP) and pan PDE4 inhibitors (rolipram) on *in vitro* and *in vivo* oligodendroglial differentiation (Syed et al., 2013; Raible and McMorris, 1993). Moreover, it has been shown that downstream of cAMP, the PKA-CREB axis is crucial for OPC differentiation, and its activation is sufficient to overcome the inhibition of myelination by fibronectin, reflective of a pathological demyelinated MS lesion (Syed et al., 2013; Raible and McMorris, 1993; Qin et al., 2017).

Next, we investigated the effects of PDE4D inhibition in an *in vivo* cuprizone model. After ceasing the cuprizone diet, both roflumilast and Gebr32a treatment were shown to enhance both molecular and functional remyelination. Both, roflumilast and Gebr32a have previously been ascribed to have pro-cognitive effects in healthy mice and an Alzheimer mouse model (Vanmierlo et al., 2016; Ricciarelli et al., 2017). However, the doses applied in the current study are not within the range of the reported spatial memory-enhancing dosages (i.e., 100-fold higher) (Vanmierlo et al., 2016; Ricciarelli et al., 2017). Besides spatial memory performances, we implemented the highly translational VEP measurements in our cuprizone animal model. VEP measurements are among of the most important electrophysiological tests for diagnosing and measuring progression during MS pathogenesis (Ridder and Nusinowitz, 2006). Abnormal latency times of VEP recordings are indicative of demyelination of the central nervous system and are highly complementary to clinical outcomes of somatosensory functions. Six weeks of cuprizone treatment significantly prolonged the latency of the VEP recordings due to the cuprizone-induced demyelination. We showed that subcutaneous treatment of 0.3 mg/kg Gebr32a successfully reduces VEP latency time in the cuprizone model. These data further support the remyelination-boosting capacity of PDE4D inhibition. Due to the lack of OPC differentiation promoting effects of the PDE4B inhibitor A33, we have not investigated its therapeutic role in the cuprizone model. However, the abovementioned finding that PDE4B inhibition skews phagocyte polarization might implicate that an indirect remyelination promoting effect of A33 could positively influence cuprizone outcome (Wang et al., 2020; Ding et al., 2021). Nevertheless, controversy exists concerning the role of macrophages for promoting repair in the cuprizone model which can be attributed, among others, to the specific therapeutic window in which compound have to be administered to observe phagocyte-mediated remyelination (Thompson and Tsirka, 2020).

On an isoform level, we demonstrate here that especially short and super-short *PDE4D* isoforms (*PDE4D1/2* and *PDE4D6*) are highly present in human MS lesion OPCs and to a lesser extent in myelinating oligodendrocytes, indicating a clear difference in cell type specific isoform

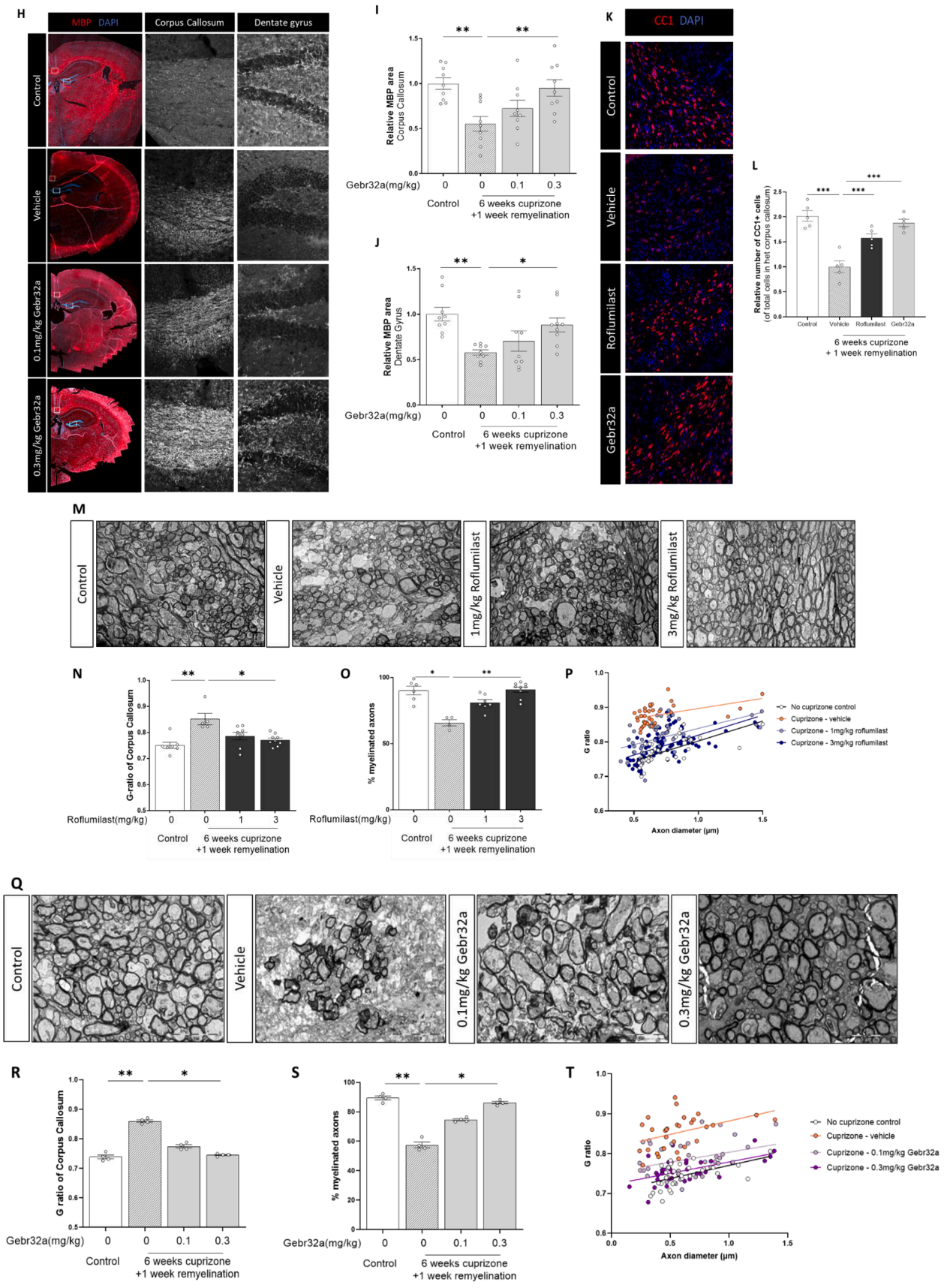

Fig. 4. (*continued*).

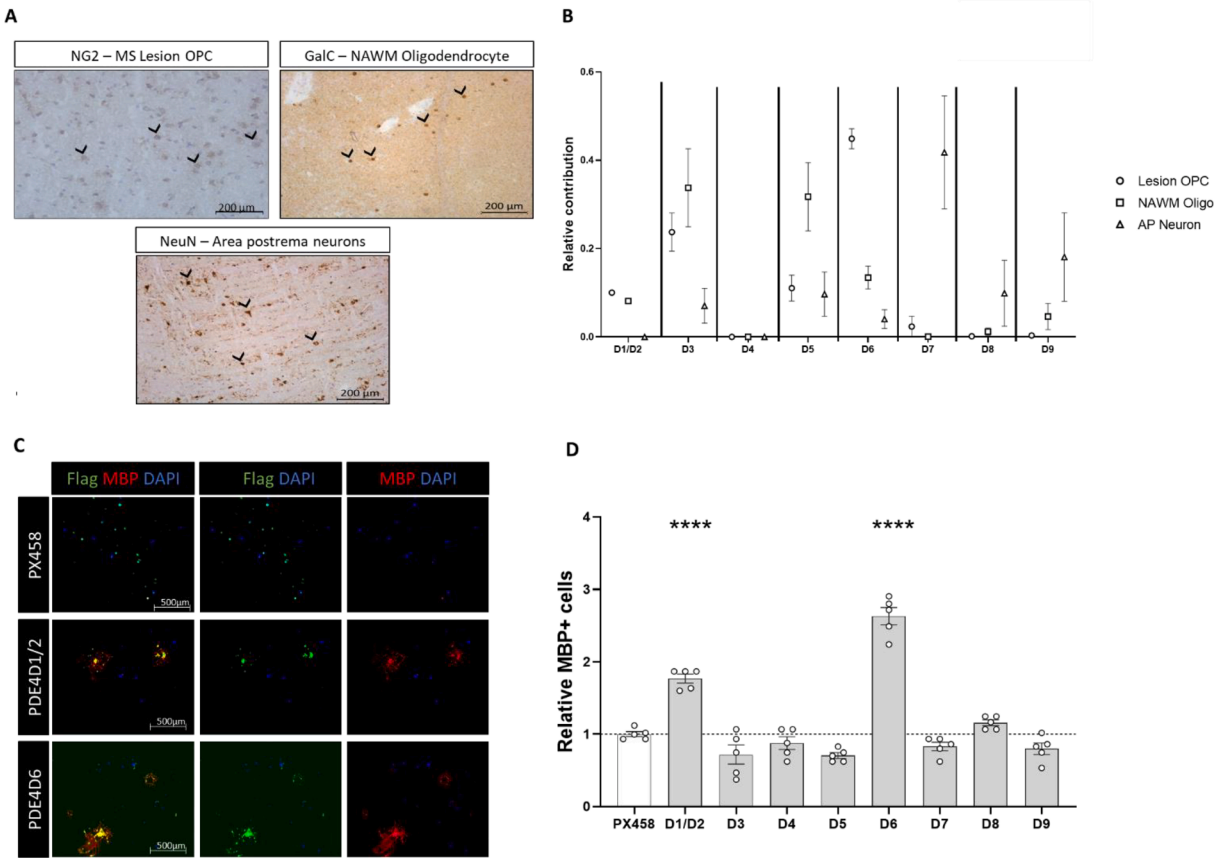

Fig. 5. Gene expression profiles of the *PDE4D* isoforms in human area postrema (AP) neurons and MS patient oligodendrocyte precursor cells (OPC) and oligodendrocytes (OLg) is indicative for biological functionality as shown by targeted isoform knockdown. (A) MS lesion OPCs, NAWM oligodendrocytes and area postrema neurons were mapped using NG2, GalC or NeuN respectively for laser capture microdissection (LCM). (B) Using LCM, 50 individually cells collected per cell type and pooled for mRNA extraction and gene expression. Oligodendrocytes and OPCs were pairwise collected in the same samples. Area postrema neurons were derived from non-neurological CNS donor samples. The proportional contribution of each splice variant was calculated for each sample (sum isoforms per sample = 1) (n = 10/group). (C-D) Primary mouse OPCs were transfected with a CRISPR/Cas9 construct (PX458 backbone with cloned gRNAs designed for specific isoform) by means of magnetofection. Fluorescence analysis showed more MBP positive oligodendrocytes within the transfected population of cells upon PDE4D1 or PDE4D6 knockdown (n = 5/group). For the LCM experiment, the sample size 'n' represents the number of donors used to isolate the belonging cell type. For the CRISPR/Cas9 experiment, the sample size 'n' represents the number of wells obtained from minimally-three independent cell culture experiments Data were analyzed using a non-parametric Kruskal-Wallis test with Dunn's multiple comparisons test (***p < 0,001).

expression abundancy. To assess the biological relevance of the individual PDE4D isoforms on OPC differentiation, we made use of a CRISPR-Cas9 genetic editing system to create isoform-specific knockdown cultures. We applied a commercially available plasmid (Ran et al., 2013), which uses a FLAG- and GFP-TAG to trace transfected cells and a Cas9 endonuclease to create a gRNA guided in/del. Transfection of primary mouse OPCs with gRNAs targeting either the short *pde4d1/2* or the super-short *pde4d6* isoform led to more MBP-positive oligodendrocytes within the transfected pool of cells, indicating that knockdown of one of the two isoforms is sufficient for boosting OPC differentiation. Importantly, no other *pde4d* isoform knockdown could significantly affect the differentiation rate of primary transfected OPCs.

As a second and more pathologically complex animal model for MS, we made use of the chronic EAE model where neuro-inflammation is the driving force of CNS demyelination. Interestingly, while lacking efficacy in the early stage of the disease, PDE4D inhibition in the chronic phase improved motor functioning and therefore lowered neurological EAE scores to the level of roflumilast-treated mice. MOG-induced neuro-inflammatory processes have been described to cause optic nerve demyelination and therefore allow remyelination assessment in the EAE model (Talla et al., 2013; Locri et al., 2018; Sekyi et al., 2021). Our findings confirm a remyelination-boosting potential of PDE4/PDE4D inhibition as lower G ratios of the optic nerve were detected, independent of the axonal diameter, in both roflumilast- and Gebr32a-treated mice at the end of the EAE experiment.

In contrast to PDE4D inhibition, PDE4B inhibition significantly reduced neuroinflammation and coinciding memory deficits and neurological scores in the acute phase of the MOG_{35-55}-induced EAE model. The cognitive deficits observed in the EAE model have previously been attributed to the up-regulation of inflammatory cytokines, dysregulation of the HPA-axis, disruption of hippocampal synapses and/or downregulation of choline acetyltransferase, all which can be influenced by altering intracellular cAMP levels (Dos Santos et al., 2019; Hou et al., 2020; Dutra et al., 2013). Post-mortem, we demonstrated a reduction in CNS-infiltrating inflammatory Th1 cells and inflammatory monocytes at EAE peak upon PDE4B inhibition. Our data corroborated these findings, as we showed an increased expression of *Arginase-1* and the anti-inflammatory cytokine *Il-27*, which additionally exerts an inhibitory function on IFN-γ production by activated $CD4^+$ T cells (Yoshimura et al., 2006; Villarino et al., 2003; Hamano et al., 2003). In line with this, PDE4B inhibition has previously been held responsible for anti-inflammatory actions (Jin et al., 2005; Ariga et al., 2004). Upon inflammatory stimulation, *Pde4b* expression is paralleled with an increase in key inflammatory markers (e.g., TNF-α and IL-1β) in immune cells including microglia, astrocytes and $CD11b^+$ macrophages (Myers et al., 2019; Avila et al., 2017). In mouse macrophages, pharmacological PDE4

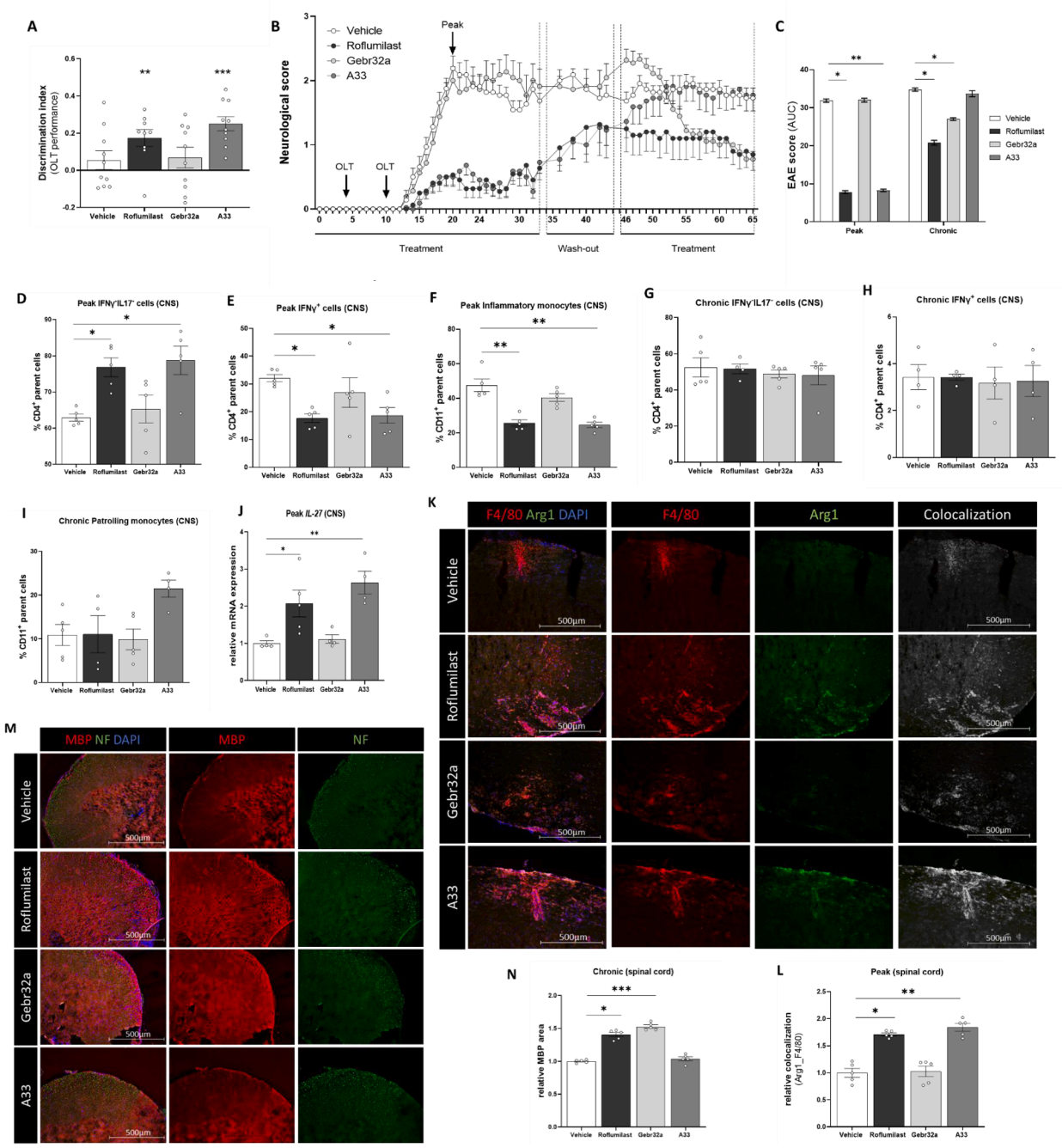

Fig. 6. Inhibition of PDE4B by A33 has immunomodulatory effects and therefore ameliorates acute clinical scores, while inhibition of PDE4D by Gebr32 reduces neurological scores in the chronic phase of the disease and enhanced the proportion of myelinated axons. (A) Four groups consisting of each 21 10-weeks old female mice were immunized with MOG_{35-55} peptide and treated with 0.1 % DMSO, roflumilast (3 mg/kg), A33 (3 mg/kg) or Gebr32a (0.3 mg/kg) by subcutaneous injections starting from the day of immunization until day 65 with a drug wash out period included from day 34–45. Preceding EAE induction, 44 out of 84 animals were trained for the object location task (OLT). After EAE induction, the 44 trained animals were subdivided among the 4 treatment groups (n = 11/group). At four and ten days post induction, preceding motor impairment, spatial memory performances were assessed using the OLT (n ≥ 8/group) (B) Animals were neurologically scored daily in a blinded manner for clinical signs on a 0–5 scale (n ≥ 9/group). (C) AUC of EAE scores were analyzed to determine significances in neurological scores (n ≥ 9/group). (D-I) At disease peak (20dpi) and at the end of the experiment (65dpi), 5 animals per group were sacrificed for flow cytometry and immunohistochemical analysis. The percentage of nonpathogenic/pathogenic T cells and inflammatory/patrolling phagocytes in the CNS are displayed in relation to the parental cells (absolute T lymphocyte and monocyte number) (n = 5/group). (J) mRNA expression analysis of *il-27* in the brain of EAE animals sacrificed at peak (n ≥ 4/group) (K-L) Longitudinal sections of the spinal cord were made at disease peak and evaluated for Arginase and F4/80 colocalization (n ≥ 4/group). (M−N) Transversal sections of the spinal cord were made at the chronic end phase of the disease where the MBP^{+} area was evaluated and correct for the number of neurofilament positive axons (n ≥ 4/group). (O-R) Optic nerves were isolated at the end of the experiment and further processed for TEM analysis (n = 5/group). A one sample *t*-test was performed to test for spatial memory (e.g. D2 ≠ 0). A non-parametric Friedman tests with Dunn's multiple comparison against vehicle group was performed to evaluate differences in clinical scores during the EAE course. The AUC of EAE scores over time, flow cytometry, IHC and TEM results were analyzed with a non-parametric Kruskal-Wallis test with Dunn's multiple comparison (*p ≤ 0,05; **p ≤ 0.01; ***p ≤ 0.001). Data shown are mean +/- SEM.

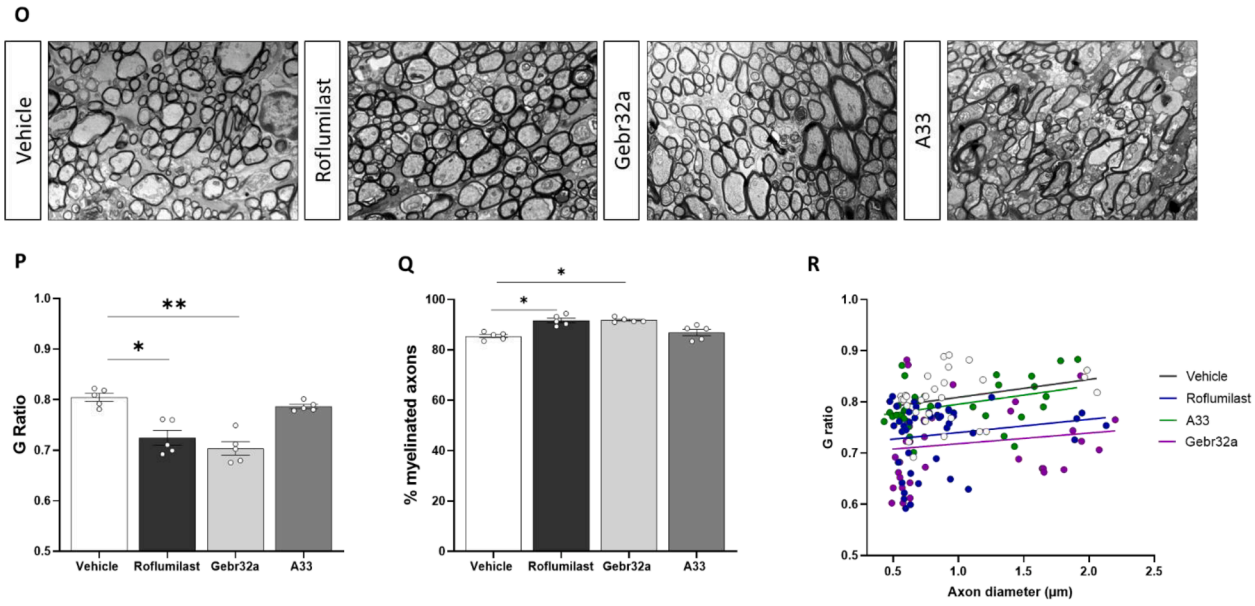

Fig. 6. (*continued*).

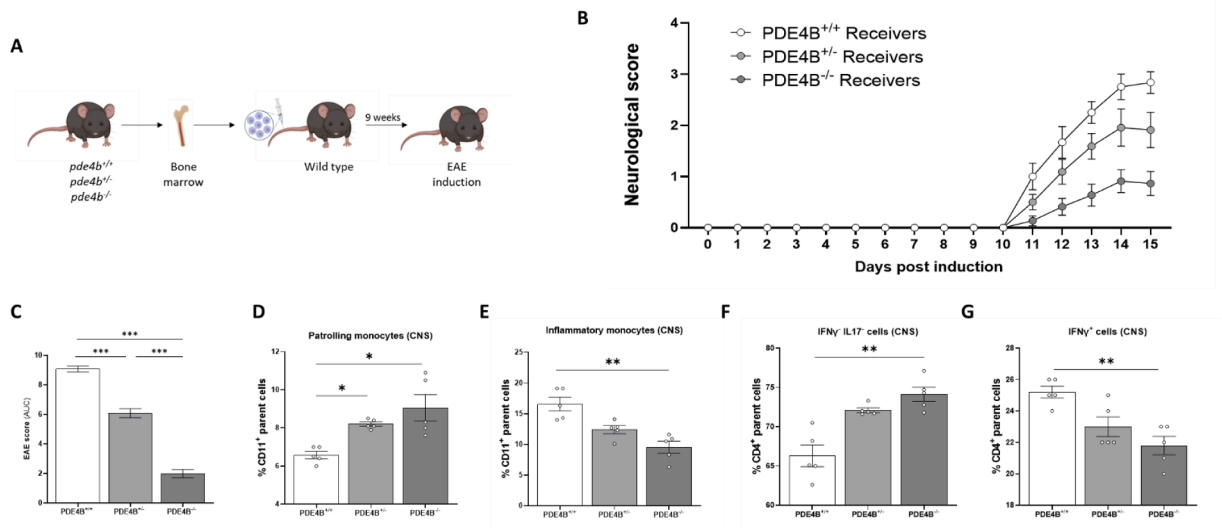

Fig. 7. Bone marrow transplantation of PDE4B$^{+/-}$ or PDEB$^{-/-}$ donors reduces neurological scores in the EAE model. (A) Schematic representation of the bone marrow transplantation followed by EAE experiment. (B) Following bone marrow transplantation and engraftment, 28 female C57bl6 OlaHsd mice were immunized in the flank and neck with MOG_{35-55} peptide emulsified in Complete Freund's Adjuvant containing Mycobacterium tuberculosis. Animals were neurologically scored for clinical signs on a daily basis ($n \geq 7$). (C) AUC of EAE scores were analyzed to determine significances in neurological scores ($n \geq 7$/group). (D-G) At the peak of the disease (15dpi), all animals were sacrificed for flow cytometry analysis. The percentage of nonpathogenic as well as pathogenic monocytes and T lymphocytes are displayed in relation to the parental cells (CD11b^{+} monocytes or CD4^{+} T lymphocytes in the CNS) ($n \geq 4$). Difference in AUC clinical scores and flow cytometry results were analyzed with a non-parametric Kruskal-Wallis test with Dunn's multiple comparison. Changes in immune cell subsets were analyzed using a non-parametric Kruskal-Wallis test with Dunn's multiple comparisons test. Data are displayed as mean +/-SEM. (*p ≤ 0,05; **p ≤ 0,01; ***p ≤ 0,005).

inhibition by rolipram (10 µM) has been shown to lower LPS-induced TNF-α production, an effect that is exclusively mediated through PDE4B-specific inhibition as demonstrated by using *Pde4b* null-macrophages (Jin et al., 2005). In line with these observations, *Pde4b*$^{-/-}$ mice highlight the crucial role of PDE4B in neuroinflammatory responses as these mice showed reduced glial cell activation upon systemic LPS-induced endotoxemia and decreased inflammatory protein markers (e.g. *GFAP, CD11b, Iba1, Cox2*) following spinal cord injury (Myers et al., 2019; Avila et al., 2017). Furthermore, intraperitoneal administration of the PDE4B inhibitor 2-(1H-indol-3-yl)-quinoxaline (derivative 3b) halted MS disease progression in the EAE zebrafish model starting from a 3 mg/kg dose (Myers et al., 2019; Sunke et al., 2019).

In line with our post-mortem results, both the pan PDE4 inhibitor rolipram and the cAMP-specific PDE7 inhibitor TC3.6 have been reported to decrease the pro-inflammatory IL-17 production and reduce the extravasation of immune cells in the CNS (Gonzalez-Garcia et al., 2013). Even though both cAMP-modulating PDE inhibitors alter the final immune response similarly, Gonzalez-Garcia et al. showed distinct pathways to achieve this immunomodulatory effect (Gonzalez-Garcia et al., 2013). The PDE7 inhibitor TC3.6 directly suppressed IL-17 production by CD4^{+} lymphocytes, while the PDE4 inhibitor rolipram only achieved this decreased production of IL-17 when CD11b + monocytes were co-cultured or when the supernatant of rolipram treated-CD11b^{+}

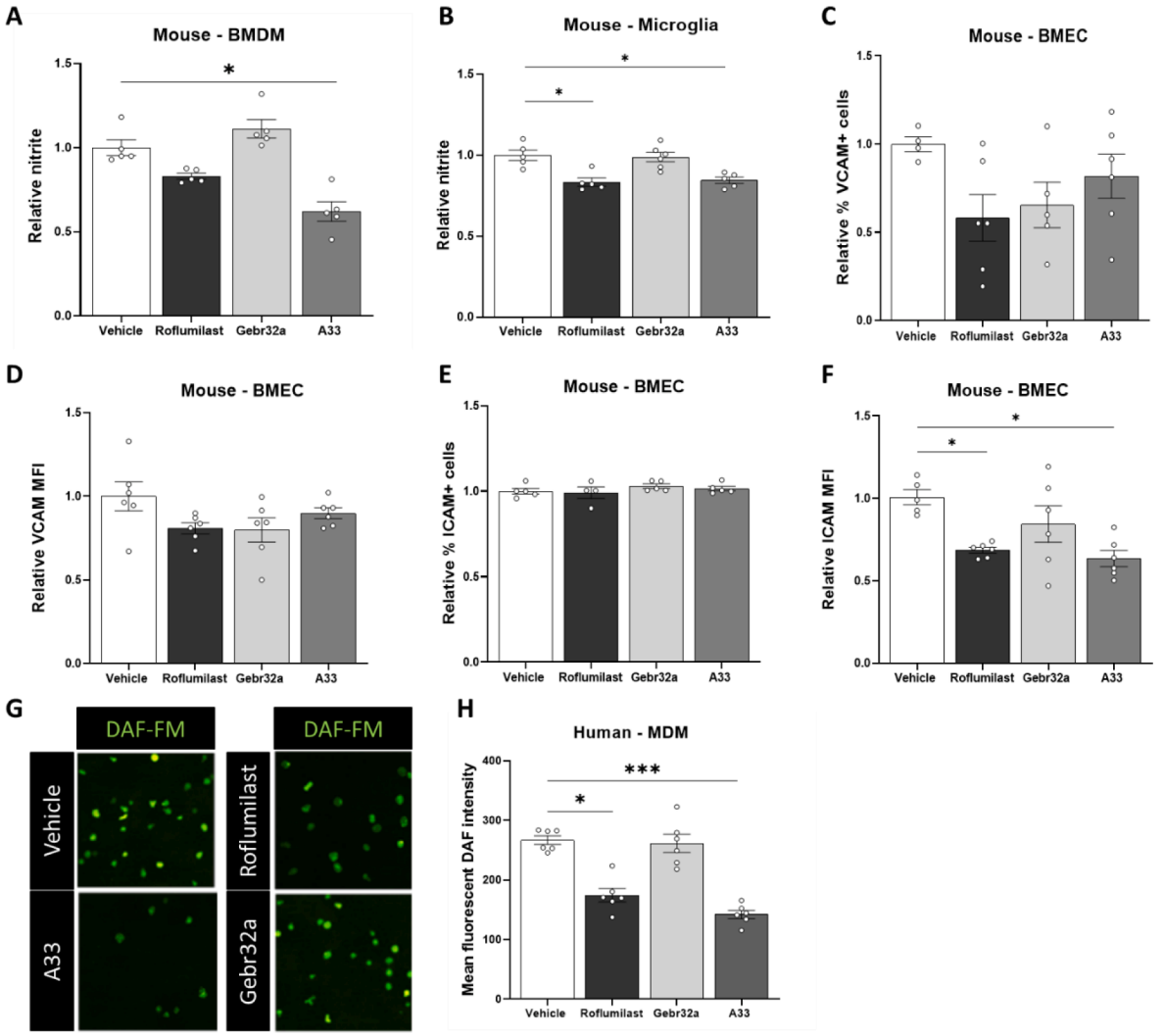

Fig. 8. Inhibition of pde4 by roflumilast and pde4b by a33 alters mouse and human phagocyte activation and lowers the mean fluorescent intensity of icam on murine endothelial cells. (a) Mouse bone marrow derived macrophages (BMDMs) or (B) microglia were stimulated with mouse myelin (100 μg/ml) for 24 h and simultaneously treated with 0.1 % DMSO, 1 μM roflumilast, 1 μM Gebr32a or 1 μM A33. After 18 h, medium was processed for NO secretion using a Griess assay (n ≥ 5/group). Furthermore, brain microvasculature endothelial cells were inflamed with TNFα (10 ng/ml) and IFNγ (10 ng/ml) and treated with the PDE4/B/D inhibitor for 48 h. Cells were harvested and adhesion molecule expression were analyzed using flow cytometry. The percentage of (C) $VCAM^+$ or (E) $ICAM^+$ positive cells and the (D and F) mean fluorescent intensity of the cells for either one of the adhesion molecules were quantified (n ≥ 4/group).(G-H) Human monocyte derived macrophages (MDMs) were stimulated with human myelin (100 μg/ml) for 24 h and simultaneously treated with 0.1 % DMSO, 1 μM roflumilast, 1 μM Gebr32a or 1 μM A33. After 18 h, human MDM cells were processed for intracellular NO production measurement using DAF-FM (n = 6/group). For the mouse BMDM, microglia and endothelial cell experiment, the sample size 'n' represents the number of wells obtained from minimally-three independent cell culture experiments. For the human MDM experiment, the sample size 'n' represents the number of donors used to isolate MDMs. Data were analyzed using a non-parametric Kruskal-Wallis test with Dunn's multiple comparisons test. Data are displayed as mean +/-SEM. (*p ≤ 0,05; ***p ≤ 0,005).

cells was transferred to the $CD4^+$ lymphocyte cultures (Gonzalez-Garcia et al., 2013). The indirect effect of rolipram on IL-17 production is thought to be mediated by monocytes' elevated production of IL-27 (Gonzalez-Garcia et al., 2013; Batten et al., 2006; Stumhofer et al., 2006). Previously, it has also been shown that the expression of the cAMP-specific PDE8A is induced in activated T lymphocytes, and inhibition of the complete PDE8 family by PF-04957325 (10 mg/kg) has been shown to suppress neuroinflammation, thereby reducing the inflammatory lesion load in the EAE animal model (Basole et al., 2022; Glavas et al., 2001). The therapeutic potential of the cAMP-specific PDE4, PDE7 and PDE8 inhibitors highlights the crucial role of cAMP in modulating the anti-inflammatory responses.

Since the inhibitors used in this study have been administered systemically, we aimed to exclude potential non-inflammatory actions because PDE4B inhibition has also been ascribed to stimulate neurogenesis, neural plasticity, synaptic strengthening and coordination of peripheral endotoxemia and gut dysbiosis - all processes which have been shown to affect inflammation and EAE outcome (Myers et al., 2019; Avila et al., 2017; Houslay et al., 2005). Therefore, we performed a BMT preceding EAE induction to target PDE4B in specifically immune cells. As with the use of a PDE4B inhibitor in the acute phase of the EAE model, selective absence of PDE4B in *pde4b*$^{-/-}$ bone marrow-transferred mice displayed a gene dosage-dependent protective effect on the neurological EAE score. Inflammatory monocytes and $INFg^+$ $CD4^+$ T cells decreased in *pde4b*$^{-/-}$ bone marrow acceptor mice, whereas patrolling phagocytes and $INFg^-IL17^-CD4^+$ T cells significantly increased during EAE.

In vitro, we have seen that phagocytes are affected by PDE4B inhibition. Human monocyte-derived macrophages and murine BMDMs, and murine microglia, which is in line with the previously reported phagocyte polarization effects of roflumilast (Santiago et al., 2018; Vilhena et al., 2021). In primary brain microvasculature endothelial

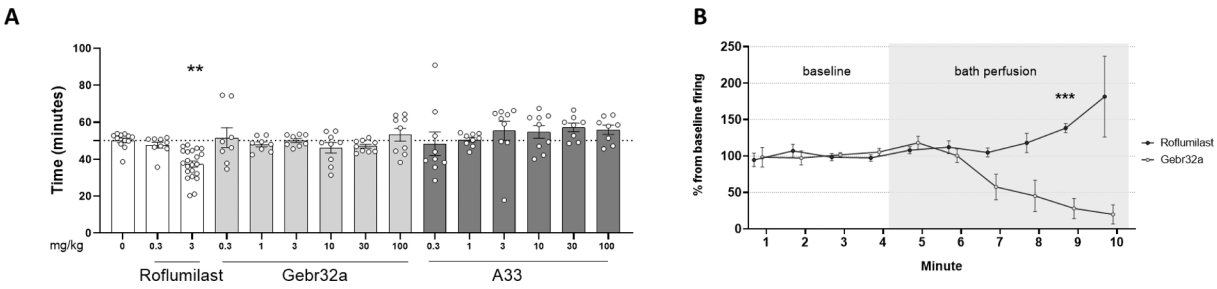

Fig. 9. The xylazine/ketamine anesthesia time and action potential firing rate of mouse area postrema neurons show no signs of emetic side effects upon PDE4B or PDE4D inhibition by means of A33 or Gebr32a. (A) Fifteen minutes following anesthesia induced by a xylazine (10 mg/kg, i.p)/ketamine (60 mg/kg, i.p) combination, mice were treated by subcutaneous injections with different doses of roflumilast (0.3 or 3 mg/kg), A33 (0.3–100 mg/kg) or Gebr32a (0.3–100 mg/kg). The time until the return of the righting reflex was used as a measure for anesthesia duration (n ≥ 8/group). (B) Putative area postrema neurons were identified based on location relative to the central canal and electrophysiological characteristics. Pipettes of 4–6 MOhm resistance filled with a Na HEPES-based solution were used for extracellular recordings using the loose cell attached method as described by (Branch and Beckstead, 2012). Baseline firing rate was recorded for four minutes. A non-parametric Kruskal Wallis test was used to evaluate significance. Data are shown as mean +/- SEM (**p ≤ 0.01;***p ≤ 0.005).

cells, a reduced protein abundance was detected at the level of ICAM-1 and subtle to no differences were detected at the level of VCAM-1 adhesion molecules, two endothelial leukocyte integrin counter-receptors that enable leukocyte transmigration to the brain (Reyes-Irisarri et al., 2007). The sole significant effect on ICAM-1 protein abundance and not on VCAM-1, nor on the percentage of cells expressing the adhesion molecules, reduces but does not exclude, the possibility of their contribution to the effects seen in the different models. Yet, since the total number of lymphocytes and monocytes were not altered in the CNS upon PDE4B inhibition, this decrease in adhesion molecule presence did not result in less immune cell infiltration and therefore contributed minimally to the PDE4B-driven protection against EAE pathology. Important to note is that we have not investigated the direct role of inhibiting PDE4B using A33 in lymphocytes. Previous research reported an essential role for cAMP modulation to alter T lymphocyte activation (Schepers et al., 2019; Koga et al., 2009). Whereas activated T lymphocytes display an enzymatic increase of PDE7, inhibiting PDE7 decreased T lymphocyte polarization and increased FoxP3 levels and anti-inflammatory IL-10 secretion (Gonzalez-Garcia et al., 2013; Smith et al., 2003; Yang et al., 2003). In line, inhibiting PDE4 displayed similar results as it reduced pro-inflammatory cytokine secretion and T lymphocyte polarization, and increased anti-inflammatory cytokine production (Gonzalez-Garcia et al., 2013; Sommer et al., 1997). Regarding the PDE4 subtypes, even though activated T lymphocytes showed an increase in enzymatic PDE4A and PDE4D levels, and not PDE4B, PDE4B was demonstrated to play an essential role in Th2 lymphocyte activation and dendritic cell recruitment (Reyes-Irisarri et al., 2007; Peter et al., 2007). However, the exact effect of inhibiting PDE4B specifically to alter T lymphocyte responses or polarization remains to be investigated.

The emetic side effects are a major drawback of the translation potential of pan PDE4 inhibitors into clinical applications. However, still a lot of controversy exists about the exact underlying mechanism of such emetic side effects. Recently, it was suggested that a reduced gastric emptying in mice upon full PDE4 inhibition was due to concurrent inhibition of more than one single PDE4 subtype since selective ablation of any PDE4 subtype did not impaired gastric emptying which was observed upon full PDE4 inhibition (McDonough et al., 2020). Nevertheless, other studies have used *pde4b*- or *pde4d*-deficient mice to determine the specific contribution of distinct subtypes in the emetic response. In contrast to *pde4b*-deficient mice, *pde4d*-deficient mice showed signs of emetic side effects since their anesthesia time was reduced in the xylazine/ketamine induced anesthesia test, a surrogate marker for measuring emesis in rodents (Robichaud et al., 2002). Furthermore, the full PDE4 inhibitor PMNPQ (0.3 mg/kg) significantly reduced anesthesia time in both wild type and *pde4b* deficient mice but did not reduce anesthesia time further in *pde4d*-deficient mice, indicating a crucial role for PDE4D in PDE4 inhibition-mediated emetic side effects (Robichaud et al., 2002). In this study, we show for the first time the *PDE4D* isoform expression profile in laser-captured neurons of the human post-mortem area postrema. Our data show that especially long PDE4D isoforms are highly concentrated in area postrema neurons and hereby highlights the importance of selectivity towards PDE4D isoforms in order to minimally alter cAMP levels in the area postrema to avoid emetogenic effects of the inhibitors. In fact, the PDE4 gene-specific inhibitors used in this study showed no emetic side effects up to 300-fold the therapeutic dose in the *in vivo* xylazine/ketamine anesthesia test, nor did they increase the action potential firing rate of mouse area postrema neurons assessed by path-clamp electrophysiology. These data already indicate a level of isoform specificity in existing inhibitors (Cavalloro et al., 2020).

Collectively, we demonstrated that specific PDE4 inhibition can orchestrate key processes in MS, such as neuroinflammation and myelin regeneration. Since full PDE4 inhibitors have been described to coincide with severe side effects, such as nausea and vomiting, new strategies should be implemented to rule out side effects while retaining potential therapeutic effects. Our data provide more insight into PDE4B inhibition to diminish neuroinflammation and isoform-specific PDE4D inhibition to stimulate remyelination. By identifying downstream isoform target specificity, non-emetogenic therapeutics can be identified and developed, since area postrema neurons show distinct expression profiles compared to oligodendroglial cells. Furthermore, as the therapeutic dose of A33 and Gebr32a used in this study already lacked emetic side effects based on murine *in vitro* and *in vivo* tests, this highlights their potential for further exploration in the context of MS and other neurodegenerative disorders.

Declaration of Competing Interest

The authors declare that they have no known competing financial interests or personal relationships that could have appeared to influence the work reported in this paper.

Data availability

The data that has been used is confidential.

Acknowledgements

MS, EP, JP and TV have a proprietary interest in selective PDE4D inhibitors for the treatment of demyelinating disorders and neurodegenerative disorders. JP has a proprietary interest in the PDE4 inhibitor roflumilast for the treatment of cognitive impairment as well as PDE4D inhibitors for the treatment of Alzheimer's disease.

We thank Prof. Dr. O.N. Viacheslav (University Medical Center Hamburg-Eppendorf, German Center for Cardiovascular Research) and Prof. Dr. M. Conti (University of California), for providing the PDE4B KO animals. Furthermore, we thank Rewind Therapeutics for providing the visual evoked potential equipment.

Funding

This work has been supported by FWO (12G0817N, 1S57521N, G041421N, and 12G0817N), Fondation Charctot Stichting (ID2020-0019), Nationale Belgische Multiple Sclerose Liga (Charco18VT), MS Liga Vlaanderen and Stichting MS Research (18-1016 MS).

Author's contributions

MS, CfC, MB, WB, AG, CV, BB, NH, JP and TV conceived the research design. MS, DP, AT, BR, EP, LvV, PG, EW, IL, PvS, EL, KW, PB, BB, and PW performed the experiments and subsequent data analysis. CB, OB, EF and RR provided research materials. MS, NH, JP and TV wrote the manuscript with input from all authors. All authors read and approved the final manuscript.

Appendix A. Supplementary data

Supplementary data to this article can be found online at https://doi.org/10.1016/j.bbi.2022.12.020.

References

Ansi Chang, M.D., Tourtellotte, W.W., Rudick, R., Trapp, D., Bruce, 2002. Premyelinating oligodendrocytes in chronic lesions of multiple sclerosis. N. Engl. J. Med. 346, 165–173.
Ariga, M., Neitzert, B., Nakae, S., Mottin, G., Bertrand, C., Pruniaux, M.P., et al., 2004. Nonredundant function of phosphodiesterases 4D and 4B in neutrophil recruitment to the site of inflammation. J. Immunol. 173 (12), 7531–7538.
Avila, D.V., Myers, S.A., Zhang, J., Kharebava, G., McClain, C.J., Kim, H.Y., et al., 2017. Phosphodiesterase 4b expression plays a major role in alcohol-induced neuro-inflammation. Neuropharmacology 125, 376–385.
Bailey, C.H., Bartsch, D., Kandel, E.R., 1996. Toward a molecular definition of long-term memory storage. PNAS 93 (24), 13445–13452.
Basole, C.P., Nguyen, R.K., Lamothe, K., Billis, P., Fujiwara, M., Vang, A.G., et al., 2022. Treatment of Experimental Autoimmune Encephalomyelitis with an Inhibitor of Phosphodiesterase-8 (PDE8). Cells 11 (4).
Batten, M., Li, J., Yi, S., Kljavin, N.M., Danilenko, D.M., Lucas, S., et al., 2006. Interleukin 27 limits autoimmune encephalomyelitis by suppressing the development of interleukin 17-producing T cells. Nat. Immunol. 7 (9), 929–936.
M. Bear BC, M. Paradiso. Neuroscience: exploring the brain. Wilkins CLW, editor2007.
Bechler, M.E., 2019. A neuron-free microfiber assay to assess myelin sheath formation. Methods Mol. Biol. 1936, 97–110.
Bielekova, B., Lincoln, A., McFarland, H., Martin, R., 2000. Therapeutic potential of phosphodiesterase-4 and -3 inhibitors in Th1-mediated autoimmune diseases. J. Immunol. 164 (2), 1117–1124.
Bielekova, B., Richert, N., Howard, T., Packer, A.N., Blevins, G., Ohayon, J., et al., 2009. Treatment with the phosphodiesterase type-4 inhibitor rolipram fails to inhibit blood–brain barrier disruption in multiple sclerosis. Mult. Scler. 15 (10), 1206–1214.
Blokland, A., Heckman, P., Vanmierlo, T., Schreiber, R., Paes, D., Prickaerts, J., 2019. Phosphodiesterase type 4 inhibition in CNS diseases. Trends Pharmacol. Sci. 40 (12), 971–985.
Bolger, G.B., 1994. Molecular biology of the cyclic AMP-specific cyclic nucleotide phosphodiesterases: a diverse family of regulatory enzymes. Cell. Signal. 6 (8), 851–859.
Branch, S.Y., Beckstead, M.J., 2012. Methamphetamine produces bidirectional, concentration-dependent effects on dopamine neuron excitability and dopamine-mediated synaptic currents. J. Neurophysiol. 108 (3), 802–809.
Braun, N.N., Reutiman, T.J., Lee, S., Folsom, T.D., Fatemi, S.H., 2007. Expression of phosphodiesterase 4 is altered in the brains of subjects with autism. Neuroreport 18 (17), 1841–1844.
Bruno, O., Fedele, E., Prickaerts, J., Parker, L.A., Canepa, E., Brullo, C., et al., 2011. GEBR-7b, a novel PDE4D selective inhibitor that improves memory in rodents at non-emetic doses. Br. J. Pharmacol. 164 (8), 2054–2063.
Cavalloro, V., Russo, K., Vasile, F., Pignataro, L., Torretta, A., Donini, S., et al., 2020. Insight into GEBR-32a: chiral resolution, absolute configuration and enantiopreference in PDE4D inhibition. Molecules 25 (4).
Charles FRJMF-C. Remyelination in the CNS: from biology to therapy. Nature Reviews Neuroscience. 2008;9:839-55.
Compston, A., Coles, A., 2008. Multiple sclerosis. Lancet 372 (9648), 1502–1517.
Cui, S.Y., Yang, M.X., Zhang, Y.H., Zheng, V., Zhang, H.T., Gurney, M.E., et al., 2019. Protection from amyloid beta peptide-induced memory, biochemical, and morphological deficits by a phosphodiesterase-4d allosteric inhibitor. J. Pharmacol. Exp. Ther. 371 (2), 250–259.
Ding, Z.B., Han, Q.X., Wang, Q., Song, L.J., Chu, G.G., Guo, M.F., et al., 2021. Fasudil enhances the phagocytosis of myelin debris and the expression of neurotrophic factors in cuprizone-induced demyelinating mice. Neurosci. Lett. 753, 135880.
Dos Santos, N., Novaes, L.S., Dragunas, G., Rodrigues, J.R., Brandao, W., Camarini, R., et al., 2019. High dose of dexamethasone protects against EAE-induced motor deficits but impairs learning/memory in C57BL/6 mice. Sci. Rep. 9 (1), 6673.
Dutra, R.C., Moreira, E.L., Alberti, T.B., Marcon, R., Prediger, R.D., Calixto, J.B., 2013. Spatial reference memory deficits precede motor dysfunction in an experimental autoimmune encephalomyelitis model: the role of kallikrein-kinin system. Brain Behav. Immun. 33, 90–101.
Fox 3rd, D., Burgin, A.B., Gurney, M.E., 2014. Structural basis for the design of selective phosphodiesterase 4B inhibitors. Cell. Signal. 26 (3), 657–663.
Fox, R.J., Coffey, C.S., Cudkowicz, M.E., Gleason, T., Goodman, A., Klawiter, E.C., et al., 2016. Design, rationale, and baseline characteristics of the randomized double-blind phase II clinical trial of ibudilast in progressive multiple sclerosis. Contemp. Clin. Trials 50, 166–177.
Fox, R.J., Coffey, C.S., Conwit, R., Cudkowicz, M.E., Gleason, T., Goodman, A., et al., 2018. Phase 2 trial of ibudilast in progressive multiple sclerosis. N. Engl. J. Med. 379 (9), 846–855.
Garcia-Leon, J.A., Garcia-Diaz, B., Eggermont, K., Caceres-Palomo, L., Neyrinck, K., Madeiro da Costa, R., et al., 2020. Generation of oligodendrocytes and establishment of an all-human myelinating platform from human pluripotent stem cells. Nat. Protoc. 15 (11), 3716–3744.
Glavas, N.A., Ostenson, C., Schaefer, J.B., Vasta, V., Beavo, J.A., 2001. T cell activation up-regulates cyclic nucleotide phosphodiesterases 8A1 and 7A3. PNAS 98 (11), 6319–6324.
Gonzalez-Garcia, C., Bravo, B., Ballester, A., Gomez-Perez, R., Eguiluz, C., Redondo, M., et al., 2013. Comparative assessment of PDE 4 and 7 inhibitors as therapeutic agents in experimental autoimmune encephalomyelitis. Br. J. Pharmacol. 170 (3), 602–613.
Hamano, S., Himeno, K., Miyazaki, Y., Ishii, K., Yamanaka, A., Takeda, A., et al., 2003. WSX-1 is required for resistance to Trypanosoma cruzi infection by regulation of proinflammatory cytokine production. Immunity 19 (5), 657–667.
Hatzelmann, A., Morcillo, E.J., Lungarella, G., Adnot, S., Sanjar, S., Beume, R., et al., 2010. The preclinical pharmacology of roflumilast–a selective, oral phosphodiesterase 4 inhibitor in development for chronic obstructive pulmonary disease. Pulm. Pharmacol. Ther. 23 (4), 235–256.
Hedde, J.R., Hanks, A.N., Schmidt, C.J., Hughes, Z.A., 2017. The isozyme selective phosphodiesterase-4 inhibitor, ABI-4, attenuates the effects of lipopolysaccharide in human cells and rodent models of peripheral and CNS inflammation. Brain Behav. Immun. 64, 285–295.
Henze, T., Rieckmann, P., Toyka, K.V., 2006. Multiple Sclerosis Therapy Consensus Group of the German Multiple Sclerosis S. Symptomatic treatment of multiple sclerosis. Multiple Sclerosis Therapy Consensus Group (MSTCG) of the German Multiple Sclerosis Society. Eur. Neurol. 56 (2), 78–105.
Hou, B., Zhang, Y., Liang, P., He, Y., Peng, B., Liu, W., et al., 2020. Inhibition of the NLRP3-inflammasome prevents cognitive deficits in experimental autoimmune encephalomyelitis mice via the alteration of astrocyte phenotype. Cell Death Dis. 11 (5), 377.
Houslay, M.D., 2010. Underpinning compartmentalised cAMP signalling through targeted cAMP breakdown. Trends Biochem. Sci 35 (2), 91–100.
Houslay, M.D., Schafer, P., Zhang, K.Y., 2005. Keynote review: phosphodiesterase-4 as a therapeutic target. Drug Discov. Today 10 (22), 1503–1519.
Jin, S.L., Lan, L., Zoudilova, M., Conti, M., 2005. Specific role of phosphodiesterase 4B in lipopolysaccharide-induced signaling in mouse macrophages. J. Immunol. 175 (3), 1523–1531.
Johnson, K.R., Nicodemus-Johnson, J., Danziger, R.S., 2010. An evolutionary analysis of cAMP-specific Phosphodiesterase 4 alternative splicing. BMC Evol. Biol. 10, 247.
Kappos, L., Bar-Or, A., Cree, B.A.C., Fox, R.J., Giovannoni, G., Gold, R., et al., 2018. Siponimod versus placebo in secondary progressive multiple sclerosis (EXPAND): a double-blind, randomised, phase 3 study. Lancet 391 (10127), 1263–1273.
Koga, K., Takaesu, G., Yoshida, R., Nakaya, M., Kobayashi, T., Kinjyo, I., et al., 2009. Cyclic adenosine monophosphate suppresses the transcription of proinflammatory cytokines via the phosphorylated c-Fos protein. Immunity 30 (3), 372–383.
Kotter, M.R., Stadelmann, C., Hartung, H.P., 2011. Enhancing remyelination in disease–can we wrap it up? Brain 134 (Pt 7), 1882–1900.
Kuhlmann, T., Miron, V., Cui, Q., Wegner, C., Antel, J., Bruck, W., 2008. Differentiation block of oligodendroglial progenitor cells as a cause for remyelination failure in chronic multiple sclerosis. Brain 131 (Pt 7), 1749–1758.
Locri, F., Cammalleri, M., Pini, A., Dal Monte, M., Rusciano, D., Bagnoli, P., 2018. Further Evidence on Efficacy of Diet Supplementation with Fatty Acids in Ocular Pathologies: Insights from the EAE Model of Optic Neuritis. Nutrients 10 (10).
Lucchinetti, C.F., Bruck, W., Rodriguez, M., Lassmann, H., 1996. Distinct patterns of multiple sclerosis pathology indicates heterogeneity on pathogenesis. Brain Pathol. 6 (3), 259–274.
Maheshwari, A., Janssens, K., Bogie, J., Van Den Haute, C., Struys, T., Lambrichts, I., et al., 2013. Local overexpression of interleukin-11 in the central nervous system limits demyelination and enhances remyelination. Mediators Inflamm. 2013, 685317.
Marenna, S., Huang, S.C., Dalla Costa, G., d'Isa, R., Castoldi, V., Rossi, E., et al., 2022. Visual evoked potentials to monitor myelin cuprizone-induced functional changes. Front. Neurosci. 16, 820155.

McDonough, W., Aragon, I.V., Rich, J., Murphy, J.M., Abou Saleh, L., Boyd, A., et al., 2020. PAN-selective inhibition of cAMP-phosphodiesterase 4 (PDE4) induces gastroparesis in mice. FASEB J. 34 (9), 12533–12548.
Mohammadnejad, A., Li, W., Lund, J.B., Li, S., Larsen, M.J., Mengel-From, J., et al., 2021. Global gene expression profiling and transcription factor network analysis of cognitive aging in monozygotic twins. Front. Genet. 12, 675587.
Mori, F., Perez-Torres, S., De Caro, R., Porzionato, A., Macchi, V., Beleta, J., et al., 2010. The human area postrema and other nuclei related to the emetic reflex express cAMP phosphodiesterases 4B and 4D. J. Chem. Neuroanat. 40 (1), 36–42.
Mosenden, R., Tasken, K., 2011. Cyclic AMP-mediated immune regulation–overview of mechanisms of action in T cells. Cell. Signal. 23 (6), 1009–1016.
Myers, S.A., Gobejishvili, L., Saraswat Ohri, S., Garrett Wilson, C., Andres, K.R., Riegler, A.S., et al., 2019. Following spinal cord injury, PDE4B drives an acute, local inflammatory response and a chronic, systemic response exacerbated by gut dysbiosis and endotoxemia. Neurobiol. Dis. 124, 353–363.
Nelissen, E., van Goethem, N.P., Bonassoli, V.T., Heckman, P.R.A., van Hagen, B.T.J., Suay, D., et al., 2019. Validation of the xylazine/ketamine anesthesia test as a predictor of the emetic potential of pharmacological compounds in rats. Neurosci. Lett. 699, 41–46.
Neyrinck, K., Garcia-Leon, J.A., 2021. Single Transcription Factor-Based Differentiation Allowing Fast and Efficient Oligodendrocyte Generation via SOX10 Overexpression. Methods Mol. Biol. 2352, 149–170.
Ontaneda, D., Thompson, A.J., Fox, R.J., Cohen, J.A., 2017. Progressive multiple sclerosis: prospects for disease therapy, repair, and restoration of function. Lancet 389 (10076), 1357–1366.
Paes, D., Schepers, M., Rombaut, B., van den Hove, D., Vanmierlo, T., Prickaerts, J., 2021. The molecular biology of phosphodiesterase 4 enzymes as pharmacological targets: an interplay of isoforms, conformational states, and inhibitors. Pharmacol. Rev. 73 (3), 1016–1049.
Peng, H., Bria, A., Zhou, Z., Iannello, G., Long, F., 2014. Extensible visualization and analysis for multidimensional images using Vaa3D. Nat. Protoc. 9 (1), 193–208.
Peng, T., Qi, B., He, J., Ke, H., Shi, J., 2020. Advances in the development of phosphodiesterase-4 inhibitors. J. Med. Chem. 63 (19), 10594–10617.
Peter, D., Jin, S.L., Conti, M., Hatzelmann, A., Zitt, C., 2007. Differential expression and function of phosphodiesterase 4 (PDE4) subtypes in human primary CD4+ T cells: predominant role of PDE4D. J. Immunol. 178 (8), 4820–4831.
Prineas, J.W., Wright, R.G., 1978. Macrophages, lymphocytes, and plasma cells in the perivascular compartment in chronic multiple sclerosis. Lab. Invest. 38 (4), 409–421.
Qin, J., Sikkema, A.H., van der Bij, K., de Jonge, J.C., Klappe, K., Nies, V., et al., 2017. GD1a overcomes inhibition of myelination by fibronectin via activation of protein kinase a: implications for multiple sclerosis. J. Neurosci. 37 (41), 9925–9938.
Raible, D.W., McMorris, F.A., 1989. Cyclic AMP regulates the rate of differentiation of oligodendrocytes without changing the lineage commitment of their progenitors. Dev. Biol. 133 (2), 437–446.
Raible, D.W., McMorris, F.A., 1993. Oligodendrocyte differentiation and progenitor cell proliferation are independently regulated by cyclic AMP. J. Neurosci. Res. 34 (3), 287–294.
Ran, F.A., Hsu, P.D., Wright, J., Agarwala, V., Scott, D.A., Zhang, F., 2013. Genome engineering using the CRISPR-Cas9 system. Nat. Protoc. 8 (11), 2281–2308.
Reyes-Irisarri, E., Sanchez, A.J., Garcia-Merino, J.A., Mengod, G., 2007. Selective induction of cAMP phosphodiesterase PDE4B2 expression in experimental autoimmune encephalomyelitis. J. Neuropathol. Exp. Neurol. 66 (10), 923–931.
Ricciarelli, R., Brullo, C., Prickaerts, J., Arancio, O., Villa, C., Rebosio, C., et al., 2017. Memory-enhancing effects of GEBR-32a, a new PDE4D inhibitor holding promise for the treatment of Alzheimer's disease. Sci. Rep. 7, 46320.
Richter, W., Menniti, F.S., Zhang, H.T., Conti, M., 2013. PDE4 as a target for cognition enhancement. Expert Opin. Ther. Targets 17 (9), 1011–1027.
Ridder 3rd, W.H., Nusinowitz, S., 2006. The visual evoked potential in the mouse–origins and response characteristics. Vision Res. 46 (6–7), 902–913.
Robichaud, A., Stamatiou, P.B., Jin, S.L., Lachance, N., MacDonald, D., Laliberte, F., et al., 2002. Deletion of phosphodiesterase 4D in mice shortens alpha(2)-adrenoceptor-mediated anesthesia, a behavioral correlate of emesis. J. Clin. Invest. 110 (7), 1045–1052.
Sanabra, C., Johansson, E.M., Mengod, G., 2013. Critical role for PDE4 subfamilies in the development of experimental autoimmune encephalomyelitis. J. Chem. Neuroanat. 47, 96–105.
Santiago, A., Soares, L.M., Schepers, M., Milani, H., Vanmierlo, T., Prickaerts, J., et al., 2018. Roflumilast promotes memory recovery and attenuates white matter injury in aged rats subjected to chronic cerebral hypoperfusion. Neuropharmacology 138, 360–370.
Schepers, M., Tiane, A., Paes, D., Sanchez, S., Rombaut, B., Piccart, E., et al., 2019. Targeting phosphodiesterases-towards a tailor-made approach in multiple sclerosis treatment. Front. Immunol. 10, 1727.
Sekyi, M.T., Lauderdale, K., Atkinson, K.C., Golestany, B., Karim, H., Feri, M., et al., 2021. Alleviation of extensive visual pathway dysfunction by a remyelinating drug in a chronic mouse model of multiple sclerosis. Brain Pathol. 31 (2), 312–332.
Shen, M.W., Arbab, M., Hsu, J.Y., Worstell, D., Culbertson, S.J., Krabbe, O., et al., 2018. Predictable and precise template-free CRISPR editing of pathogenic variants. Nature 563 (7733), 646–651.
Shi, Y., Lv, J., Chen, L., Luo, G., Tao, M., Pan, J., et al., 2021. Phosphodiesterase-4D knockdown in the prefrontal cortex alleviates memory deficits and synaptic failure in mouse model of alzheimer's disease. Front. Aging Neurosci. 13, 722580.
Sierksma, A.S., van den Hove, D.L., Pfau, F., Philippens, M., Bruno, O., Fedele, E., et al., 2014. Improvement of spatial memory function in APPswe/PS1dE9 mice after chronic inhibition of phosphodiesterase type 4D. Neuropharmacology 77, 120–130.
Smith, S.J., Brookes-Fazakerley, S., Donnelly, L.E., Barnes, P.J., Barnette, M.S., Giembycz, M.A., 2003. Ubiquitous expression of phosphodiesterase 7A in human proinflammatory and immune cells. Am. J. Physiol. Lung Cell. Mol. Physiol. 284 (2), L279–L289.
Sommer, N., Martin, R., McFarland, H.F., Quigley, L., Cannella, B., Raine, C.S., et al., 1997. Therapeutic potential of phosphodiesterase type 4 inhibition in chronic autoimmune demyelinating disease. J. Neuroimmunol. 79 (1), 54–61.
Sonar, S.A., Lal, G., 2017. Differentiation and transmigration of CD4 T cells in neuroinflammation and autoimmunity. Front. Immunol. 8, 1695.
Stumhofer, J.S., Laurence, A., Wilson, E.H., Huang, E., Tato, C.M., Johnson, L.M., et al., 2006. Interleukin 27 negatively regulates the development of interleukin 17-producing T helper cells during chronic inflammation of the central nervous system. Nat. Immunol. 7 (9), 937–945.
Sunke, R., Bankala, R., Thirupataiah, B., Ramarao, E., Kumar, J.S., Doss, H.M., et al., 2019. InCl3 mediated heteroarylation of indoles and their derivatization via CH activation strategy: Discovery of 2-(1H-indol-3-yl)-quinoxaline derivatives as a new class of PDE4B selective inhibitors for arthritis and/or multiple sclerosis. Eur. J. Med. Chem. 174, 198–215.
Syed, Y.A., Baer, A., Hofer, M.P., Gonzalez, G.A., Rundle, J., Myrta, S., et al., 2013. Inhibition of phosphodiesterase-4 promotes oligodendrocyte precursor cell differentiation and enhances CNS remyelination. EMBO Mol. Med. 5 (12), 1918–1934.
Talla, V., Yu, H., Chou, T.H., Porciatti, V., Chiodo, V., Boye, S.L., et al., 2013. NADH-dehydrogenase type-2 suppresses irreversible visual loss and neurodegeneration in the EAE animal model of MS. Mol. Ther. 21 (10), 1876–1888.
Thompson, K.K., Tsirka, S.E., 2020. Guanabenz modulates microglia and macrophages during demyelination. Sci. Rep. 10 (1), 19333.
Tiane, A., Schepers, M., Riemens, R., Rombaut, B., Vandormael, P., Somers, V., et al., 2021. DNA methylation regulates the expression of the negative transcriptional regulators ID2 and ID4 during OPC differentiation. Cell. Mol. Life Sci. 78 (19–20), 6631–6644.
Trojano, M., Paolicelli, D., Bellacosa, A., Cataldo, S., 2003. The transition from relapsing-remitting MS to irreversible disability: clinical evaluation. Neurol. Sci. 24 (Suppl 5), S268–S270.
Ugarte, A., Gil-Bea, F., Garcia-Barroso, C., Cedazo-Minguez, A., Ramirez, M.J., Franco, R., et al., 2015. Decreased levels of guanosine 3', 5'-monophosphate (cGMP) in cerebrospinal fluid (CSF) are associated with cognitive decline and amyloid pathology in Alzheimer's disease. Neuropathol. Appl. Neurobiol. 41 (4), 471–482.
Vanmierlo, T., Rutten, K., Dederen, J., Bloks, V.W., van Vark-van der Zee, L.C., Kuipers, F., et al., 2011. Liver X receptor activation restores memory in aged AD mice without reducing amyloid. Neurobiol. Aging 32 (7), 1262–1272.
Vanmierlo, T., Creemers, P., Akkerman, S., van Duinen, M., Sambeth, A., De Vry, J., et al., 2016. The PDE4 inhibitor roflumilast improves memory in rodents at non-emetic doses. Behav. Brain Res. 303, 26–33.
Vilhena, E.R., Bonato, J.M., Schepers, M., Kunieda, J.K.C., Milani, H., Vanmierlo, T., et al., 2021. Positive effects of roflumilast on behavior, neuroinflammation, and white matter injury in mice with global cerebral ischemia. Behav. Pharmacol. 32 (6), 459–471.
Villarino, A., Hibbert, L., Lieberman, L., Wilson, E., Mak, T., Yoshida, H., et al., 2003. The IL-27R (WSX-1) is required to suppress T cell hyperactivity during infection. Immunity 19 (5), 645–655.
Wang, S.S., Bi, H.Z., Chu, S.F., Dong, Y.X., He, W.B., Tian, Y.J., et al., 2020. CZ-7, a new derivative of Claulansine F, promotes remyelination induced by cuprizone by enhancing myelin debris clearance. Brain Res. Bull. 159, 67–78.
Weiner, H.L., 2009. The challenge of multiple sclerosis: how do we cure a chronic heterogeneous disease? Ann. Neurol. 65 (3), 239–248.
Whitaker, C.M., Beaumont, E., Wells, M.J., Magnuson, D.S., Hetman, M., Onifer, S.M., 2008. Rolipram attenuates acute oligodendrocyte death in the adult rat ventrolateral funiculus following contusive cervical spinal cord injury. Neurosci. Lett. 438 (2), 200–204.
Wilson, N.M., Gurney, M.E., Dietrich, W.D., Atkins, C.M., 2017. Therapeutic benefits of phosphodiesterase 4B inhibition after traumatic brain injury. PLoS One 12 (5), e0178013.
Wingerchuk, D.M., Carter, J.L., 2014. Multiple sclerosis: current and emerging disease-modifying therapies and treatment strategies. Mayo Clin. Proc. 89 (2), 225–240.
Wolinsky, J.S., Arnold, D.L., Brochet, B., Hartung, H.P., Montalban, X., Naismith, R.T., et al., 2020. Long-term follow-up from the ORATORIO trial of ocrelizumab for primary progressive multiple sclerosis: a post-hoc analysis from the ongoing open-label extension of the randomised, placebo-controlled, phase 3 trial. Lancet Neurol. 19 (12), 998–1009.
Wolswijk, G., 1998. Chronic stage multiple sclerosis lesions contain a relatively quiescent population of oligodendrocyte precursor cells. J. Neurosci. 18 (2), 601–609.
Wouters, K., Cudejko, C., Gijbels, M.J., Fuentes, L., Bantubungi, K., Vanhoutte, J., et al., 2012. Bone marrow p16INK4a-deficiency does not modulate obesity, glucose homeostasis or atherosclerosis development. PLoS One 7 (3), e32440.
Wucherpfennig, K.W., Newcombe, J., Li, H., Keddy, C., Cuzner, M.L., Hafler, D.A., 1992. T cell receptor V alpha-V beta repertoire and cytokine gene expression in active multiple sclerosis lesions. J. Exp. Med. 175 (4), 993–1002.
Xiang, J., Wang, X., Gao, Y., Li, T., Cao, R., Yan, T., et al., 2020. Phosphodiesterase 4D gene modifies the functional network of patients with mild cognitive impairment and Alzheimer's disease. Front. Genet. 11, 890.
Yang, J.X., Hsieh, K.C., Chen, Y.L., Lee, C.K., Conti, M., Chuang, T.H., et al., 2017. Phosphodiesterase 4B negatively regulates endotoxin-activated interleukin-1 receptor antagonist responses in macrophages. Sci. Rep. 7, 46165.

Yang, G., McIntyre, K.W., Townsend, R.M., Shen, H.H., Pitts, W.J., Dodd, J.H., et al., 2003. Phosphodiesterase 7A-deficient mice have functional T cells. J. Immunol. 171 (12), 6414–6420.

Yoshimura, T., Takeda, A., Hamano, S., Miyazaki, Y., Kinjyo, I., Ishibashi, T., et al., 2006. Two-sided roles of IL-27: induction of Th1 differentiation on naive CD4+ T cells versus suppression of proinflammatory cytokine production including IL-23-induced IL-17 on activated CD4+ T cells partially through STAT3-dependent mechanism. J. Immunol. 177 (8), 5377–5385.

Zawadzka, M., Rivers, L.E., Fancy, S.P., Zhao, C., Tripathi, R., Jamen, F., et al., 2010. CNS-resident glial progenitor/stem cells produce Schwann cells as well as oligodendrocytes during repair of CNS demyelination. Cell Stem Cell 6 (6), 578–590.

Zhang, C., Cheng, Y., Wang, H., Wang, C., Wilson, S.P., Xu, J., et al., 2014. RNA interference-mediated knockdown of long-form phosphodiesterase-4D (PDE4D) enzyme reverses amyloid-beta42-induced memory deficits in mice. J. Alzheimers Dis. 38 (2), 269–280.

Zhang, C., Xu, Y., Zhang, H.T., Gurney, M.E., O'Donnell, J.M., 2017. Comparison of the pharmacological profiles of selective PDE4B and PDE4D inhibitors in the central nervous system. Sci. Rep. 7, 40115.

Zhang, C., Xu, Y., Chowdhary, A., Fox 3rd, D., Gurney, M.E., Zhang, H.T., et al., 2018. Memory enhancing effects of BPN14770, an allosteric inhibitor of phosphodiesterase-4D, in wild-type and humanized mice. Neuropsychopharmacology 43 (11), 2299–2309.